

1 **Reconstruction of Temperature, Accumulation Rate,**
2 **and Layer Thinning from an Ice Core at South Pole**
3 **Using a Statistical Inverse Method**

Emma C. Kahle¹, Eric J. Steig¹, Tyler R. Jones², T.J. Fudge¹, Michelle R.

Koutnik¹, Valerie A. Morris², Bruce H. Vaughn², Andrew J. Schauer¹, C.

Max Stevens¹, Howard Conway¹, Edwin D. Waddington¹, Christo Buizert³,

Jenna Epifanio³, James W. C. White²

4 ¹Department of Earth and Space Sciences, University of Washington, Seattle WA 98195, USA

5 ²Institute of Arctic and Alpine Research, University of Colorado, Boulder CO 80309, USA

6 ³College of Earth Ocean and Atmospheric Sciences, Oregon State University, Corvallis OR 97331, USA

7 **Contents of this file**

8 1. Text S1 to S5

9 2. Figures S1 to S19

Corresponding author: Emma C. Kahle, Department of Earth and Space Sciences, University
of Washington, Seattle WA 98195, USA. (eckahle@uw.edu)

10 **Introduction.** This supporting information document provides further details on meth-
11 ods used in the analysis described in the main text. We include information about:

12 S1. Diffusion-length data and modeling

13 S2. Inverse methods

14 S3. Sensitivity tests

15 S4. Ice-flow modeling

16 S5. The $\delta^{15}\text{N}$ -based thinning function

17 **Text S1. Diffusion-length data and modeling**

18 *S1.1 Corrections to diffusion-length data*

19 We make two corrections to the estimates of diffusion length calculated from the spectra
20 of the water-isotope data.

21 First, we correct for the effect on the water-isotope data from the continuous-flow-analysis
22 (CFA) measurement system. As melted ice samples are transported through the tubing
23 and reservoirs of the CFA system, some smoothing of the high-frequencies of the natural
24 water-isotope variations occurs. This smoothing is minimized by design of the components
25 of the CFA-system, but still impacts the measured signal. The extent of this system
26 smoothing can be quantified by measuring the system response to a step change in isotopic
27 value using laboratory-produced ice (Jones et al., 2017b). The system diffusion length for
28 the CFA system used in this analysis is 0.07 cm for $\delta^{17}\text{O}$ and $\delta^{18}\text{O}$, and 0.08 cm for δD
29 (Jones et al., 2017b).

30 Second, we correct for the additional diffusion that occurred in the solid ice below the
31 bottom of the firn, following Gkinis et al. (2014). To calculate the solid-ice diffusion length,
32 we assume the modern borehole temperature profile $T(z)$ remains constant through time
33 to find the diffusivity profile $D_{ice}(z)$, following Gkinis et al. (2014):

$$D_{ice}(z) = 9.2 \times 10^{-4} \times \exp\left(\frac{-7186}{T(z)}\right), \quad (1)$$

34 with $T(z)$ given in K and $D_{ice}(z)$ given in $\text{m}^2 \text{s}^{-1}$. For $T(z)$ at SPC14, we use borehole
35 temperature measurements from the nearby neutrino observatory (Price et al., 2002).

36 The solid-ice diffusion length is also affected by vertical strain in the ice sheet. We assume
 37 a simple thinning function from a 1-D ice-flow model (Dansgaard and Johnsen, 1969) with
 38 a kink-height $h_0 = 0.2$ for this calculation. We describe the total thinning experienced by
 39 a layer $S(t)$ in a given time interval $t = 0$ to $t = t'$ as:

$$S(t') = \exp\left(\int_0^{t'} \dot{\epsilon}_z(t) dt\right), \quad (2)$$

40 where $\dot{\epsilon}_z(t)$ is the vertical strain rate calculated from the thinning function. The solid-ice
 41 diffusion length, σ_{ice} , is then calculated as (Gkinis et al., 2014):

$$\sigma_{ice}^2(t') = S(t')^2 \int_0^{t'} 2D_{ice}(t)S(t)^{-2} dt. \quad (3)$$

42 To produce the corrected diffusion-length data set used in this analysis, we subtract in
 43 quadrature both the system diffusion length, σ_{CFA} , and the solid-ice diffusion length,
 44 σ_{solid} , from the total measured diffusion length, σ_{meas} :

$$\sigma^2 = \sigma_{meas}^2 - \sigma_{CFA}^2 - \sigma_{solid}^2. \quad (4)$$

45 The diffusion length σ represents the diffusion that occurred within the firn column and
 46 that has experienced the effects of vertical strain in the ice sheet (*i.e.*, $\sigma = S(z)\sigma_{firn}$).
 47 Figure S1 shows the effect of these corrections on the estimated diffusion length.

48 *S1.2 Modeling firn diffusion length*

49 Within the forward model of the inverse problem, we model diffusion length in the firn
 50 column. We use the following values in calculating the diffusivity coefficients, D_x , for each
 51 water-isotope ratio:

$$D_{\delta^{18}O}^{air} = \frac{D^{air}}{1.0285} \quad (\text{Johnsen et al., 2000}) \quad (5)$$

$$D_{\delta^{17}O}^{air} = \frac{D^{air}}{1.01466} \quad (\text{Luz and Barkan, 2010}) \quad (6)$$

$$D_{\delta D}^{air} = \frac{D^{air}}{1.0251} \quad (\text{Johnsen et al., 2000}) \quad (7)$$

52 where:

$$D^{air} = 0.211 \times 10^{-4} \times \left(\frac{T}{273.15} \right)^{1.94} \times \frac{P_0}{P} \quad (\text{Johnsen et al., 2000}) \quad (8)$$

53 is the diffusivity of water vapor in air. T is temperature given in Kelvin and P is the
54 atmospheric pressure compared to a reference pressure of $P_0 = 1$ atm.

55 We use the following values in calculating the fractionation factors, α_x , for each water-
56 isotope ratio, for the equilibrium of water vapor over ice:

$$\alpha_{18} = \exp\left(\frac{11.839}{T} - 28.224 \times 10^{-3}\right) \quad (\text{Majoube, 1970}) \quad (9)$$

$$\alpha_{17} = \exp(0.529 \times \log(\alpha_{18})) \quad (\text{Barkan and Luz, 2007}) \quad (10)$$

$$\alpha_D = \exp\left(-0.0559 + \frac{13525}{T^2}\right) \quad (\text{Lamb et al., 2017}) \quad (11)$$

57 The tortuosity parameter τ used in Equation 5 in the main text is given by (Schwander
58 et al., 1988; Johnsen et al., 2000):

$$\frac{1}{\tau} = \begin{cases} 1 - b \times \left(\frac{\rho}{\rho_{ice}} \right)^2 & , \text{ for } \rho \leq \frac{\rho_{ice}}{\sqrt{b}} \\ 0 & , \text{ for } \rho > \frac{\rho_{ice}}{\sqrt{b}} \end{cases} \quad (12)$$

59 using a tortuosity parameter $b = 1.3$.

The solution to Equation 4 in the main text for the isotope profile at a given depth z and time t is given by:

$$\delta(z, t) = S(t) \frac{1}{\sigma\sqrt{2\pi}} \int_{-\infty}^{\infty} \delta(z, 0) \exp\left(\frac{-(z-u)^2}{2\sigma^2}\right) du, \quad (13)$$

as described in (Gkinis et al., 2014) and fully derived in Kahle et al. (2020), where σ is the diffusion length and the factor $S(t)$ is the total thinning a layer has experienced due to ice flow, as described in Equation 2 of this supplement.

Text S2. Inverse methods

The statistical inverse method used in this work relates the three variables that span the model space with the three data variables that span the data space. We define the model space as a vector space with a dimension for each of the unknown input parameters; a particular point in the model space represents a specific set of input parameters m . The data space is defined similarly, where each data parameter in d represents a dimension, and our observations d_{obs} exist at a particular point in the data space. Because the data have measurement uncertainties, the “true” values in the data space may differ from d_{obs} . Because we have three model parameters across 208 depth points (624 total unknown parameters), our problem spans a high dimensional model space, and an exhaustive search of all possible solutions m is not practical. We limit the number of instances of m to evaluate by using an importance-sampling algorithm. We use a Markov Chain Monte Carlo algorithm to combine *a priori* information about which solutions m are plausible for realistic ice-sheet conditions and information from our data sets. This algorithm efficiently explores the parameter space by favoring instances of m that are similar to those that have already produced good fits with the observations d_{obs} .

79 In this section, we describe the theoretical framework (S2.1 and S2.2) and the practical
 80 implementation (S2.3) of the inverse approach we use. In general, the solution of this type
 81 of inverse problem depends on the formulation of the problem, including what information
 82 is included in the constraints and how the output is analyzed. We detail below each of
 83 the choices that we make in our approach.

84 *S2.1 Bayesian framework*

85 We use a statistical Bayesian framework to solve this inverse problem. Rather than seek a
 86 single best-fit solution, we consider the likelihood of different solutions based on probabil-
 87 ity distributions within the parameter spaces of the data and the model. This framework
 88 combines *a priori* model parameter information with data measurement uncertainties.
 89 Unlike a regularization approach, such as Tikhonov regularization, a Bayesian approach
 90 does not require a subjective choice about how well the final set of solutions should fit
 91 the data (Tarantola, 1987; Steen-Larsen et al., 2010).

92 We characterize the *a priori* information describing the model inputs m as a probability
 93 distribution in the model space. This distribution, denoted as $\rho_m(m)$, represents the
 94 likelihood of solutions m based on data-independent prior knowledge about what values
 95 are realistic for that particular parameter (Mosegaard and Tarantola, 1995; Mosegaard
 96 & Sambridge, 2002). To produce the complete solution to the problem, the *a priori*
 97 information is combined with the likelihood function, which describes how well the output
 98 d from a given solution $G(m)$ matches our observations d_{obs} . The likelihood function $L(m)$
 99 is defined as (Mosegaard and Tarantola, 1995):

$$L(m) = C_L \exp(-M(m)), \tag{14}$$

100 where C_L is a normalization constant and $M(m)$ is a misfit function that measures the
 101 deviation between d and d_{obs} in the data space.

102 The likelihood function $L(m)$ is combined with the *a priori* distribution $\rho_m(m)$ to define
 103 the *a posteriori* distribution $f(m)$ (Tarantola, 1987):

$$f(m) = C_f L(m) \rho_m(m). \quad (15)$$

104 Note that in our implementation, detailed in S2.3, we directly incorporate *a priori* in-
 105 formation into the model space bounds and thus directly compare values of the misfit
 106 function $M(m)$ calculated for each solution m . Specific values for C_L , C_f , and ρ_m are not
 107 required.

108 The *a posteriori* distribution $f(m)$ contains all the information we have to constrain
 109 the inverse problem and thus represents its complete solution. The region of maximum
 110 values of $f(m)$ denote the most likely solutions to the problem. This distribution may be
 111 Gaussian-like and simple to interpret, or may be multi-modal and require a more complex
 112 interpretation. We cannot produce this *a posteriori* distribution analytically, but we can
 113 sample its values at discrete points. For each solution m that we test in our forward model
 114 G , we calculate a discrete value of $f(m)$.

115 *S2.2 Sampling strategy*

116 Our sampling strategy uses an algorithm to determine which solutions m to test, with
 117 the goal of producing $f(m)$ after sufficient iterations (Mosegaard and Tarantola, 1995).
 118 The algorithm explores the model space by randomly stepping from one solution m_i to
 119 a neighbor m_j . In each iteration, the algorithm follows two stages, designed such that it
 120 asymptotically produces $f(m)$ (Mosegaard, 1998; Mosegaard & Sambridge, 2002).

121 First, an exploration stage defines how the algorithm selects a proposal for m_j given its
 122 starting place at m_i . The selection depends on how far in model space the algorithm
 123 is allowed to step in a single iteration. While the magnitude and direction of the step
 124 are determined randomly, the magnitude is scaled by a base step-size. The choice of
 125 base step-size balances the exploration of more of the model space (larger steps) with the
 126 exploration of regions that result in high values of $f(m)$ (smaller steps). In practice, we
 127 must tune the step size in order to strike this balance (*e.g.*, Steen-Larsen et al. (2010)).

128 Second, an exploitation stage defines the transition probability that the proposed step
 129 will be accepted. If the proposed step is rejected, the current solution m_i is repeated for
 130 an additional iteration. The simplest choice for the transition probability is the Metropo-
 131 lis acceptance probability (Metropolis et al., 1953; Mosegaard, 1998; Mosegaard & Sam-
 132 bridge, 2002):

$$p_{\text{accept}} = \min \left(1, \frac{f(m_j)}{f(m_i)} \right). \quad (16)$$

133 This formulation will always accept the proposed step to m_j if the *a posteriori* distribution
 134 is greater at that point ($f(m_j) > f(m_i)$), but may still accept the proposed step even if
 135 the *a posteriori* distribution is smaller at that point ($f(m_j) < f(m_i)$) by a probability
 136 proportional to $\frac{f(m_j)}{f(m_i)}$. This design prevents the algorithm from getting stuck at a local
 137 maximum of $f(m)$, while still favoring samples from regions of the model space with a
 138 relatively high value of $f(m)$.

139 After sufficient iterations, the sampling of this algorithm will converge on $f(m)$. The
 140 number of iterations required for convergence, the convergence time, depends on the base
 141 step-size chosen. Step size is tuned to minimize the number of iterations required while

142 appropriately sampling the model space. Related to the convergence time is the burn-in
143 time, which refers to the number of iterations completed before the sampled values of
144 $f(m)$ become relatively stationary. After this point, the algorithm continues to sample
145 only highly likely solutions m . Prior work has found that after the burn-in time, the
146 acceptance rate of the algorithm should be 25-50% (Gelman et al., 1996) in order to strike
147 a balance between exploration (bigger steps) and efficiency (smaller steps).

148 *S2.3 Implementation of sampling*

149 To sample and estimate the *a posteriori* distribution, we implement the theory described
150 above. We initiate the problem with our initial guess m_1 for each parameter and begin
151 evaluating successive solutions from that point. Our sampling strategy uses Equation 16
152 and the associated ideas about sampling efficiency.

153 In the exploration stage of the algorithm, rather than perturb only one parameter within
154 m_i at a time, all 624 parameters (*i.e.*, values at each depth point for temperature, ac-
155 cumulation rate, and thinning function) are perturbed in each iteration. This design
156 improves the efficiency of the algorithm. Each perturbation is constructed with the same
157 low-frequency, red-noise slope in its power spectral density as that of a comparison data
158 set. The comparison data set for temperature is the water-isotope record, for accumu-
159 lation rate is a destrained version of the annual-layer thicknesses, and for the thinning
160 function is a DJ-model output. Because in reality we expect temperature, accumulation
161 rate, and thinning to vary smoothly through time, each proposed perturbation must vary
162 smoothly as well. Furthermore, the Δ age and diffusion-length data sets are inherently
163 smooth because they integrate information over the depth of the firn column. To pre-

164 vent spurious high-frequency noise from being introduced into the proposed solution m ,
 165 we apply a low-pass filter to the perturbation. To the temperature and accumulation-
 166 rate perturbations, we apply a lowpass filter at a 3000-year period, which corresponds
 167 to the maximum value of Δage . We apply a lowpass filter at a 10,000-year period to
 168 the thinning-function perturbations because we expect the thinning function to be even
 169 smoother. The perturbations are then added to the previous accepted solution to generate
 170 the next proposed solution.

171 In the exploitation stage, the algorithm determines whether to accept the proposed solu-
 172 tion m_{i+1} by calculating and comparing the values of the *a posteriori* distribution at m_i
 173 and m_{i+1} . Equation 15 describes how the *a posteriori* distribution is calculated from the
 174 likelihood function $L(m)$ and the *a priori* distribution $\rho(m)$. Because we have already in-
 175 corporated our prior knowledge directly into the model space bounds, we simply compare
 176 the value of the likelihood function evaluated at m_i and m_{i+1} (Mosegaard, 1998):

$$p_{\text{accept}} = \min \left(1, \frac{L(m_{i+1})}{L(m_i)} \right). \quad (17)$$

177 We define the likelihood function, as in Equation 14, with a misfit function $M(m)$ defined
 178 as (Khan et al., 2000; Mosegaard & Sambridge, 2002):

$$M(m) = \sum_n \frac{|d^{(n)}(m) - d_{\text{obs}}^{(n)}|}{\sigma_n}, \quad (18)$$

179 where $d^{(n)}(m)$ denotes the modeled output, $d_{\text{obs}}^{(n)}$ the observation, and σ_n the standard de-
 180 viation of the observation for the n th datum. This misfit function minimizes the influence
 181 of outliers, compared to a root-mean-square formulation.

182 We run the algorithm until we have 100,000 accepted samples of the *a posteriori* distribu-
 183 tion. With an acceptance rate of 30-40%, this requires approximately 300,000 iterations

184 in total. The burn-in time is reached after approximately 10,000 iterations, and we con-
185 sider solutions m only after this point. We repeat this process five times to account for
186 any persistent impacts from early perturbations, combining all accepted solutions after
187 the burn-in time to create the final set of results. Because only a small perturbation is
188 made between iterations, successive iterations are correlated. Analysis of the *a posteriori*
189 distribution requires a collection of statistically independent models, so we consider only
190 a subset of all accepted models (Mosegaard, 1998; Dahl-Jensen et al., 1998). Through an
191 autocorrelation analysis of the accepted models, we conclude that saving every 300th solu-
192 tion produces a statistically independent set. Out of a total of 500,000 accepted solutions,
193 1500 solutions are included in our analysis of the *a posteriori* distribution.

194 **Text S3. Sensitivity tests**

195 *S3.1 Sensitivity to Firn Model*

196 To evaluate the sensitivity of the results to the choice of firn model, we perform two
197 sets of experiments comparing different firn models. First, we use the Community Firn
198 Model (CFM) (Stevens et al., 2020; Gkinis et al., 2021) to calculate Δage using our full
199 ensemble of accumulation-rate and temperature reconstructions as inputs for five different
200 models: a dynamic version of Herron-Langway, Goujon et al. (2003), Li and Zwally (2015),
201 Ligtenberg et al. (2011), and Simonsen et al. (2013). (Solving the full inverse problem
202 with any of these dynamic models, which do not have analytical solutions, is impractical,
203 but we address this issue in the second set of experiments below.) Comparison of the
204 outputs of the five different models and the Δage data is given in Figure S2. The results
205 show that while the Ligtenberg et al. (2011) and Li and Zwally (2015) models produce

206 similar results for the glacial period, the Goujon et al. (2003) and Simonsen et al. (2013)
207 models systematically underestimate Δage by about 500 years. As currently formulated,
208 none of these models other than Herron-Langway are consistent with the modern depth-
209 density profiles at South Pole. Because the accumulation rate and thinning function are
210 tightly constrained by the diffusion-length and layer-thickness data, the only available
211 free parameter that could be used to reconcile these other models with the empirical
212 Δage data is temperature. For the Goujon et al. (2003) model, for example, adjusting
213 the temperature to match Δage requires reducing the temperature by about 2°C in the
214 glacial and by $> 3^\circ\text{C}$ in the Holocene; the latter is implausible and would require an even
215 smaller glacial-interglacial temperature change than our reconstruction indicates. Thus,
216 our choice of Herron-Langway is motivated by the fact that it produces results most
217 consistent with multiple, independent, empirical constraints.

218 In a second set of experiments, we further examine the sensitivity of our results to the
219 choice of firn model by implementing two of the models, Goujon et al. (2003) (GOU) and
220 Ligtenberg et al. (2011) (LIG), within our inverse model framework. These two models are
221 representative end-members (Figure S2). We use the CFM to run these models to steady
222 state using a range of temperature and accumulation-rate pairs that span the climate of
223 the SPC14 record. We save the model output in a format that is accessible from within
224 the inverse procedure, allowing the appropriate firn age-depth-density profile to be used
225 for the corresponding temperature and accumulation-rate value in each iteration.

226 Figure S3 shows the results of these experiments compared with the main result using the
227 Herron-Langway analytic model (HLA). Both the GOU and LIG firn models produce lower
228 temperatures throughout the record, lower accumulation-rate values in the Holocene, and

229 slightly higher thinning function values through the Holocene and glacial transition, com-
230 pared to the main HLA result. Although the Last Glacial Maximum (LGM) temperature
231 in the GOU and LIG results is lower than that of the HLA result, the glacial-interglacial
232 temperature change is similar for all three models, as shown in Figure S4. This shows
233 that the relatively small glacial-interglacial change, one of the key results in this paper, is
234 not a consequence of our model choice. Building on the result of the first set of firn-model
235 experiments, it also further demonstrates that the HLA model is an appropriate model
236 for South Pole.

237 *S3.2 Sensitivity to Measured Data Sets*

238 To determine the extent to which each of our three data sets affects the results, we
239 tested our approach by excluding different combinations of the data sets. We used the
240 same inverse framework as before, but took into account only how well the output d
241 matches the data observations d_{obs} for the data sets included in that test. Excluding all
242 data sets evaluates the effect of the perturbation construction by resampling the *a priori*
243 distribution (Mosegaard and Tarantola, 2002). Figure S5 illustrates that this null test, in
244 which there are *no* constraints from the data, successfully recovers the prior; the mean
245 of the *a priori* distribution is approximately the mean of the bounded model space. This
246 result shows that no spurious information is produced by the sampling procedure.

247 Building up from the null test, we tested two suites of three runs each to evaluate the
248 sensitivity of results to each of the data sets. The first suite includes only one data set
249 at a time, and the second suite includes two data sets at a time. The results from both
250 suites are similar, and we show here only the results from the second. Figure S6 shows

251 the mean solution from each run of the second suite: excluding Δ age (purple), excluding
252 diffusion length (blue), and excluding layer thickness (green), compared alongside the
253 full results including all parameters (black). The right three panels show the effect on
254 the fit of the data parameters, producing, as expected, the worst fit to each data set
255 when that information is excluded from the problem. The left three panels of Figure S6
256 show how the exclusion of each data set impacts the mean of each set of solutions. The
257 result for the thinning function suggests that, from 40 - 54 ka, the diffusion-length record
258 pulls the thinning function to greater values (less thinning), while the layer thickness
259 pulls the thinning function to smaller values (more thinning). The accumulation-rate
260 reconstruction is most sensitive to diffusion length and layer thickness. To assess the
261 sensitivity of the temperature reconstruction, we ran our two suites of sensitivity tests
262 again, this time prescribing accumulation rate to the mean solution. Figure S7 shows the
263 results for temperature for each of the four types of tests. The results suggest that Δ age
264 is most important for temperature at ages younger than 35 ka. At ages older than 35 ka,
265 no single data set is most important for temperature, but the results of the 2-parameter
266 suite suggest that the combined information from diffusion length and layer thickness has
267 the greatest impact on the temperature result.

268 Additionally, we tested the impact of the diffusion-length data set on the temperature re-
269 sult by isolating the temperature-dependence of the water-isotope diffusion model within
270 the forward model. We used a linear step-change input for temperature within the diffu-
271 sion model (solid magenta line in temperature panel of Figure S8), not allowing changes
272 of temperature in each iteration to influence the misfit of the modeled diffusion lengths to
273 the data set. These results (blue shading in Figure S8) show a significant difference in the

274 results for all three variables (temperature, accumulation rate, and thinning function),
275 particularly during the LGM. This occurs because the fixed temperature we use for the
276 diffusivity increases the modeled firn diffusion length, requiring more thinning to match
277 the diffusion-length data. To accommodate the increased thinning, accumulation rate
278 must increase to match the layer-thickness data. To compensate for a higher accumula-
279 tion rate, a colder temperature is required to match the Δage data. In this particular
280 example, the glacial-interglacial temperature change is reduced by 1.4°C from the main
281 results, a significant difference. Setting a constant diffusion temperature colder than the
282 main result would have the opposite effect. This sensitivity test demonstrates that the
283 water-isotope diffusion model provides a critical constraint on temperature, comparable
284 in significance to Δage .

285 *S3.3 Sensitivity to $\delta^{15}\text{N}$ data*

286 As detailed in Section 5.4 of the main text, we use the $\delta^{15}\text{N}$ -based diffusive column height
287 (DCH) to assess the impact of the $\delta^{15}\text{N}$ data on our main result. We run a global search
288 algorithm over a range of temperature and accumulation-rate values to find those that are
289 in agreement with the $\delta^{15}\text{N}$ -based DCH. The temperature and accumulation-rate values
290 included in our global search are defined by a small range about the corresponding mean
291 values in the main reconstruction. For temperature values, we define the range as $\pm 5^\circ\text{C}$,
292 and for accumulation-rate values, we define the range as $\pm 0.01 \text{ m a}^{-1}$. Given the variability
293 in each parameter, the temperature range is relatively larger than the accumulation-rate
294 range, which is appropriate since the accumulation rate is fairly well constrained.

295 Accompanying Figure 5 in the main text, Figure S9 shows the DCH as calculated with
296 the accumulation-rate and temperature results shown in Figure 5. The red shading,
297 corresponding to the red shading in Figure 5, shows the DCH calculated when the $\delta^{15}\text{N}$
298 constraint is applied to the accumulation rate and temperature solutions. The red shading
299 exactly spans the uncertainty of the $\delta^{15}\text{N}$ -based DCH, demonstrating that the solutions
300 shown in Figure 5 are consistent with the $\delta^{15}\text{N}$ data. A change in the global search ranges
301 of temperature and accumulation-rate has a minor effect on the width of the red shading,
302 but no impact on the mean values. We note that the equivalent representation of the blue
303 shading from Figure 5 in Figure S9 is identical to that of the red shading.

304 As noted in the main text, these results show that the Herron-Langway firn model (and all
305 other firn models we examined) cannot simultaneously accommodate all data constraints
306 at all depths. We emphasize that while $\delta^{15}\text{N}$ tightly constrains the DCH, $\delta^{15}\text{N}$ does not
307 depend on the details of the depth-density profile, nor on the amount of time represented
308 by the DCH, and therefore cannot constrain either of these variables independently. In
309 contrast, Δage is a measure of the firn densification time, and water-isotope diffusion
310 length depends on both the densification time and the depth-density structure. Within
311 the firn-model framework, warmer temperatures than our main reconstruction permit
312 agreement with $\delta^{15}\text{N}$, but reduce agreement with diffusion-length constraints. We consider
313 our reconstruction conservative with respect to the key result of a relatively warm last
314 glacial maximum. We suggest that water-isotope diffusion-length data, such as we present
315 in this paper, should be used to a greater extent in developing further refinements to firn
316 models in the future (Gkinis et al., 2021).

317 *S3.4 Sensitivity of Isotope-Temperature Relationship*

318 In Section 6.2 of the main text, we show that the $\delta^{18}\text{O}$ -temperature relationship indicated
319 by our reconstruction, based on the HL firn model, is $0.99\text{‰}\text{C}^{-1}$. Table S1 shows results of
320 the same calculation for the sensitivity tests using other firn models (Figure S3), and from
321 the $\delta^{15}\text{N}$ and Δage constraints (main text Figure 5). We also report the correlation coef-
322 ficient r between the $\delta^{18}\text{O}$ record and each temperature reconstruction. All $\partial(\delta^{18}\text{O})/\partial T$
323 slopes are significantly greater than the modern surface slope of $0.8\text{‰}\text{C}^{-1}$. While all
324 correlations are significant, the maximum correlation is for the main reconstruction.

325 **Text S4. Ice-flow modeling**

326 We use a 2.5-D flowband ice-flow model to estimate a thinning function for SPC14 to
327 compare with the primary thinning function reconstruction described in the main text.
328 As described in the main text, the primary thinning reconstruction contains more high-
329 frequency variation than a 1-D Dansgaard-Johnsen model output. For emphasis, Fig-
330 ure S10 shows this comparison in the depth domain to highlight the main discrepancies
331 in the estimates, particularly from 200 to 500 m depth and from 1400 to 1750 m depth.
332 This ice-flow-model thinning function is constrained by data for ages younger than 10 ka,
333 producing an independent data-based estimate of ice thinning. Beyond 10 ka, we do not
334 have sufficient knowledge of past ice flow direction and the associated bed topography
335 along that flow path in order to fully constrain the model. For the older ice, the goal
336 with the ice-flow-model thinning function is to determine if the structure in the primary
337 thinning function is physically plausible. To this end, our flowband modeling suggests
338 that variations in the primary thinning function can indeed be explained by observed
339 variations in bedrock topography.

340 *S4.1 Flowband model*

341 The flowband model was developed to calculate the time-dependent ice-surface evolution
342 and velocity distribution along a flowline in the ice-sheet interior. The model has been
343 described in Koutnik et al. (2016) where it was applied near the WAIS Divide ice-core
344 site. The model calculates the ice-flow field using the Shallow Ice Approximation, which
345 is appropriate for relatively slow-flowing interior ice that is not beneath an ice divide.
346 Necessary boundary conditions and initial inputs to the model include the accumulation
347 rate (Figure S11A), bed topography (Figure S11C), and ice temperature along the flowline,
348 as well as the ice flux and ice-sheet thickness at one location.

349 The flow field described by the model is defined within a flowband domain extending
350 200 km along the flow line. The downstream edge of the domain is located 10 km from
351 the SPC14 site; the upstream edge marks the location of the ice divide, 190 km upstream
352 of the SPC4 site. The width of the flowband domain (Figure S11B) is a tunable parameter
353 and is determined such that the model matches the measured surface velocities and surface
354 elevations described below (Text S4.2). The ice flux and ice-surface elevation are specified
355 at one point in the domain, which we chose to be near to the drill site.

356 For this work, we calculate a steady-state flow field, rather than consider the transient
357 response to time-varying forcing. A steady-state model is justified for three main reasons.
358 First, the steady-state model provides a good fit to the observed depth-age relationship
359 for the Holocene (Figure S12), where the flowline location and corresponding bed topog-
360 raphy are well defined. The steady-state model also compares well with the ice advection
361 estimated by Lilien et al. (2018) (Figure S13), which included a $\sim 15\%$ speed up of sur-

362 face ice over the last 10 ka. Second, temporal variations in the accumulation rate have
363 little impact on the cumulative thinning as a function of depth (*e.g.*, Nye, 1963). We
364 calculate the thinning as a function of depth and then convert to a function of age based
365 on the SP19 timescale (Winski et al., 2019). Third, while accumulation-rate variations
366 and other changes to the boundary conditions affect ice-particle-path trajectories, these
367 inputs require knowledge of the flowline and bed topography, which are poorly known
368 beyond 65 km upstream from SPC14. Without specification of where the ice flowed, we
369 cannot determine these time-variable inputs, and a time-dependent model has limited
370 value. Additionally, we find that a steady-state model satisfies our goal of evaluating the
371 physical plausibility of the primary thinning function reconstruction.

372 *S4.2 Model Inputs*

373 *Velocity, elevation, spatial pattern of accumulation rate, and flowline determination:* Mea-
374 surements of the surface velocity, surface elevation, and the determination of the flowline
375 from these measurements are described in Lilien et al. (2018), with data available from
376 the United States Antarctic Program Data Center (USAP-DC) at: [https://www.usap-
377 dc.org/view/project/p0000200](https://www.usap-dc.org/view/project/p0000200). The surface velocity was measured at a network of stakes
378 with 12.5 km spacing along the lines of longitude every 10° from 110° E to 180° E and
379 out to a distance of 100 km from SPC14. The modern surface velocities were used to
380 determine the modern flowline. The accumulation-rate pattern along the flowline (Figure
381 S11A) was inferred using traced layers imaged with a 200 MHz radar. By comparing the
382 measured layer thickness in SPC14 to the expected layer thickness due to advection of
383 the upstream accumulation-rate pattern, the flowline was confidently determined for a

384 distance of 65 km upstream of SPC14, spanning the past 10.1 ka (Lilien et al., 2018). For
385 ice older than 10 ka, we are uncertain what path the ice took.

386 *Bedrock topography:* The bed topography along the domain of the flowline (from SPC14
387 to the ice divide) is a necessary model input, and can be grouped into three sections
388 based on the data available (Figure S11C). 1) From 0 to 65 km upstream of SPC14,
389 we are confident that the ice flowed over the bedrock topography imaged with radar
390 along the modern flowline. 2) For 65 km to 100 km upstream from SPC14, we use the
391 bedrock topography measured along the modern flowline; however, we cannot be sure
392 that ice reaching the SPC14 site flowed along this path. 3) From 100 km to a divide at
393 approximately 190 km upstream, we have no information about the modern flowline, nor
394 do we know the bed topography. However, we can obtain a plausible example of the bed
395 topography from an airborne radar survey in this region.

396 For the first and second sections, the bedrock topography along 100 km of the modern flow-
397 line upstream of SPC14 was imaged with a ground-based, bistatic impulse radar with cen-
398 ter frequency of 7 MHz (Figure S14). The radar system has been used widely in Antarctica
399 (Gades et al., 2000; Neumann et al., 2008; Catania et al., 2010). The radar data and bed
400 picks are posted at the USAP-DC at: <https://www.usap-dc.org/view/project/p0000200>.

401 For the third section, to provide additional information about the spatial variability in the
402 bed topography beyond 100 km, we use the PolarGAP airborne radar survey (Forsberg
403 et al., 2017). Although PolarGAP data were collected along 135° E and 142.5° E (Figure
404 S14), the data are publicly available as a gridded product. We interpolate the gridded
405 data to extract the bed topography along the two flight lines. The bed topography along

our flowline and the two PolarGAP lines are shown in Figure S15. The three profiles track together well until about 70 km upstream of SPC14 where they diverge as the spacing between the lines increases. To obtain a model input for bed topography that produces thinning variations similar to the primary thinning function (recall that our goal is to evaluate whether these variations are physically plausible), we combine information from the two PolarGAP lines. We connect two points (green circles in Figures S15 and S16) that yield a flowline over a high in the bed topography. The orientation of this flowline is nearly perpendicular to the modern flowline, so the ice is unlikely to have flowed over it; however, this example illustrates that the magnitude of topographic variation required to match the structure of the primary thinning function does exist in the region.

Ice temperature: An ice-temperature profile is specified using a 1-D thermal model fit to the measurements from the AMANDA and IceCube projects (Price et al., 2002), forced to reach the pressure melting point at the bed. This temperature profile is held constant in time and is scaled linearly as a function of ice thickness along the flowline to estimate the full temperature field in our model domain.

Basal melt rate: We test two choices for basal melt rate to gain insight into the sensitivity of the thinning result to this parameter. With all other parameters taken to be the same, one case has no basal melt and one case has 1 cm a^{-1} of basal melt across the whole domain. A 1 cm a^{-1} melt rate is similar to the value inferred by Jordan et al. (2018) farther upstream of SPC14. The difference between the resulting thinning functions increases with depth, but differs by only 17% during the last 10,000 years of the core. For simplicity, we plot only the non-basal melt result in Figure 6 of the main text.

428 *S4.3 Tuning the model*

429 The flux out the downstream edge of the domain was specified to obtain a velocity of
430 10 m a^{-1} to match modern observations (Lilien et al., 2018). To approximately match the
431 velocities measured at 12.5 km intervals out to a farthest distance of 100 km upstream
432 (Figure S11E), the width of the flowband was increased with distance upstream (Fig-
433 ure S11B). This represents convergent flow, as indicated for this region from the surface
434 topography. The velocity measurements (Lilien et al., 2018) are not precise enough to al-
435 low reliable convergence estimates, and we therefore assumed a linear change in flowband
436 width for 100 km upstream. Beyond 100 km upstream, the flowband width continues
437 to increase, at a different rate, such that the divide position is approximately 190 km
438 upstream at an elevation of 3075 m, consistent with a likely ice origin at Titan Dome
439 (Fudge et al., 2020).

440 *S4.4 Comparison with measured layers*

441 The modeled layers are shown in comparison to 7 internal layers imaged by radar (Figure
442 S17). There is a good fit at the core site, which is also reflected in Figure S12, comparing
443 the modeled depth-age profile and the measured data from SP19. The match to the radar
444 layers is not nearly as good upstream where the amplitude of the modeled layers at the
445 bedrock bump is less than what is observed in the measured layers. The discrepancy may
446 be related to the greater uncertainty in the flowband model inputs farther upstream from
447 SPC14.

448 *S4.5 Ice-flow-model thinning function*

449 The ice-flow-model thinning function (Figure 6 in main text) is calculated from the mod-
450 eled layer thickness at the core site divided by the original thickness (the accumulation
451 rate) when that ice was deposited at the surface. The numerical calculation can become
452 noisy due to the finite model mesh and the difficulty of establishing the accumulation rate
453 at the point of origin given variations in the surface accumulation pattern. Therefore,
454 we smooth the thinning function with a moving average over a depth interval of 50 m.
455 The jaggedness of the thinning function is the most noticeable in the deepest layers where
456 there are smaller depth differences for the same age interval. Because we have used a
457 steady-state model, the modeled age for a given depth is too young for ages prior to the
458 Holocene (since we do not account for the lower accumulation rates of the glacial pe-
459 riod). Because the cumulative thinning as a function of depth is insensitive to temporal
460 variations in accumulation (*e.g.*, Nye, 1963), we convert modeled depth to age using the
461 measured depth-age relationship (SP19; Winski et al. (2019)).

462 The most prominent feature in the thinning function calculated for the Holocene period
463 is at about 7 ka. The ~ 7 ka layers have thinned less than the layers above, which we
464 term a “reversal” in the thinning function; for example, Parrenin et al. (2004) noted
465 such features for the Vostok ice core. For SPC14, reversals can occur because the strain
466 thinning of layers is affected by changes in ice thickness along the flow line (Figure S18).
467 As the ice flows from a bedrock high into a trough, the thickening of the ice column
468 either reduces the vertical thinning or can even cause vertical thickening. Therefore, ice
469 parcels reaching the ~ 7 ka layer have thinned less than if the bedrock were flat because
470 the ice column thickened. Ice parcels reaching younger layers, for example the 6 ka layer,
471 have not experienced this thickening. As the ice flows out of this overdeepening, the rise

472 in bed topography causes thinning of the full ice column (*i.e.*, both the 6 ka and 7 ka
 473 particles). For the bed topography along the flowline spanning the Holocene time period
 474 (from SPC14 to 65 km upstream), this bed overdeepening is the only feature that has a
 475 significant impact on the structure of the thinning function.

476 **Text S5. $\delta^{15}\text{N}$ -based thinning function**

477 We use a thinning function estimated from measurements of $\delta^{15}\text{N}$ in SPC14 for an ad-
 478 ditional comparison with the primary thinning function reconstruction described in the
 479 main text (Figure 6 in main text). Following Parrenin et al. (2012), the $\delta^{15}\text{N}$ -based thin-
 480 ning function uses the diffusive column height as calculated from the $\delta^{15}\text{N}$ measurements
 481 and the Δdepth as calculated from the ice age scale to determine how much thinning has
 482 occurred since that ice was at the surface (see main text Section 6.1).

483 We calculate the DCH with (Parrenin et al., 2012):

$$\text{DCH}(t) = (\delta^{15}\text{N}(t) - \Omega(T)\Delta T_{diff}) \left(\frac{\Delta m g \times 1000}{RT(t)} \right)^{-1}, \quad (19)$$

484 where $\Omega(T)$ is the thermal diffusivity, T_{diff} is the temperature difference between the top
 485 and bottom of the diffusive column, Δm is the difference in molar mass between ^{15}N and
 486 ^{14}N in kg mol^{-1} , g is the gravitational acceleration (9.81 m s^{-2}), R is the gas constant
 487 ($8.314 \text{ J mol}^{-1} \text{ K}^{-1}$), and $T(t)$ is the temperature history in K. We use the temperature
 488 reconstruction from the optimization in the main text to estimate the temperature history.
 489 The temperature difference in the firn is calculated using a 1-D ice-and-heat flow model
 490 (Fudge et al., 2019), also forced by the accumulation-rate reconstruction. The temperature
 491 dependence of the thermal diffusivity is from Grachev and Severinghaus (2003).

492 The Δdepth is conceptually similar to the Δage except that it is the difference in depth in
 493 the core, rather than age, of the same climate event in the ice and gas phases. The Δdepth
 494 is found for each gas tie point used to develop the SP19 gas timescale (Epifanio et al.,
 495 2020). The depth of the ice of the same age is then found from the SP19 ice timescale
 496 (Winski et al., 2019).

497 The $\delta^{15}\text{N}$ -based thinning function (Γ) can be described:

$$\Gamma(t) = \frac{\Delta\text{depth}(t)}{\int_0^{\text{LID}(t)} D(z, t) dz} = \frac{\Delta\text{depth}(t)}{\text{LIDIE}(t)} = \frac{\Delta\text{depth}(t)}{A \times \text{LID}(t)}, \quad (20)$$

498 where

$$\text{LID}(t) = \text{DCH}(t) + \text{CZ} = \text{DCH}(t) + 3. \quad (21)$$

499 $D(z, t)$ is the density profile of the firn relative to density of ice at a given time, $\text{LID}(t)$ is
 500 the lock-in depth, $\text{LIDIE}(t)$ is the lock-in depth in ice equivalent, $\text{DCH}(t)$ is the diffusive
 501 column height, and CZ is the thickness of the convective zone, which we set to 3 m (a
 502 typical value found in firn air pumping experiments).

503 Parrenin et al. (2012) showed that the LID/LDIE ratio changes relatively little for different
 504 climate conditions at Dome C and thus we can use a constant factor to convert LID to
 505 LIDIE . We obtain a value of $A=0.717$ by integrating the SPC14 density profile (Winski
 506 et al., 2019) from the surface to a density of 824 kg m^{-3} . In the following sections, we
 507 discuss the primary sources of uncertainty in the $\delta^{15}\text{N}$ -based thinning function.

508 *S5.1 Uncertainties*

509 We estimate the uncertainties in the calculation of this thinning function by calculating the
510 change in the thinning function with a different input for the seven main parameters below
511 (Figure S19). We choose values which we believe yield approximately 95% confidence (*i.e.*,
512 2 standard deviation).

513 *Density and depth of firn column:* Converting the LID to LIDIE has two primary un-
514 certainties: uncertainty in the measured modern density profile and how much variation
515 there is through time. We estimate the first using six firn cores, two at SPC14 and two
516 near South Pole, as well as two at 50 km upstream (Lilien et al., 2018). We assume lock-in
517 density at 824 kg m^{-3} with an uncertainty $\pm 5 \text{ kg m}^{-3}$. The conversion factor, A , to get
518 LIDIE from LID is equivalent to the average density of the firn column relative to the
519 density of ice, and hence is unitless. To estimate the uncertainty of this conversion factor
520 A , we find a maximum difference of 0.015 among the six firn cores relative to measured
521 value for SPC14.

522 For the time-varying uncertainty in the conversion factor A , we use the pairs of temper-
523 ature and accumulation rate for each time step found in the primary reconstruction to
524 force a Herron-Langway densification model. We also allow the surface density to vary by
525 $\pm 30 \text{ kg m}^{-3}$ from the SPC14 surface density value. We find the largest difference from
526 the modern SPC14 value to define an uncertainty of 0.023 (2 standard deviation).

527 *Convective zone impact on diffusive column height:* The modern convective zone is 3 m
528 and we assume the uncertainty is ± 3 m.

529 *Vertical thinning of firn column due to ice flow:* Separate from firn compaction, there
530 is vertical thinning caused by the lateral stretching due to ice flow and the effectively

531 incompressible nature of ice under these conditions. Measurements of englacial vertical
532 velocities have become possible with phase sensitive radars; however, separating the ver-
533 tical thinning due to ice flow from the vertical compaction of the firn is not yet possible.
534 Therefore, we approximate this vertical thinning assuming a uniform, ice-equivalent ver-
535 tical strain rate (*e.g.*, Nye, 1963). We develop the uncertainty by assuming either no
536 vertical thinning or double our default vertical thinning.

537 *Δ depth:* We estimate the uncertainty of the Δ depth from the Δ age uncertainties devel-
538 oped for the SP19 gas timescale (Epifanio et al., 2020). To find the uncertainty, we take
539 the difference in depths that correspond to the maximum and minimum gas ages and
540 divide it in half.

541 *Measurement uncertainty and variability:* The DCH is calculated from the $\delta^{15}\text{N}$ of N_2 data
542 using Equation 19. The uncertainty in determining the DCH depends on three things:
543 1) the measurement uncertainty of the $\delta^{15}\text{N}$; 2) variability in how well the measurement
544 represents the actual DCH; and 3) the uncertainty in interpolation from the closest mea-
545 surement. The $\delta^{15}\text{N}$ has been measured at 50- to 100-year resolution for much of the
546 core, such that the interpolation distances are small. To jointly assess these measurement
547 uncertainty and variability, we compared the DCH estimates of the three closest mea-
548 surements. On average, the three measurements differed by slightly less than 2 m. The
549 differences among the three measurements did not have a temporal trend, so we calculate
550 the uncertainty with a constant 2 m uncertainty. This is the smallest uncertainty for most
551 of the measurements.

552 *Thermal fractionation:* The thermal fractionation of $\delta^{15}\text{N}$ is calculated using a 1-D ice-
553 and-heat flow model (Fudge et al., 2019). The firn-density profile is assumed constant
554 through time, with the temperature and accumulation-rate histories from the main re-
555 construction presented here as the primary forcings. The thermal conductivity in the firn
556 follows the Van Dusen formula (Cuffey and Paterson, 2010). The temperature difference is
557 calculated from top and bottom of the diffusive column. The isothermal diffusive column
558 height is used initially in the temperature difference calculation; a new diffusive column
559 height is computed including thermal fractionation and the temperature difference is then
560 recalculated. One iteration is sufficient to reach a stable diffusive column height. The
561 amount of thermal fractionation increases in the glacial compared to the Holocene. This
562 is driven by the lower glacial accumulation rates, which decrease the vertical advection in
563 the firn column. Because the base of the firn column is warmer than the surface, warming
564 will tend to mute the temperature gradient in the firn, while cooling will enhance the
565 temperature gradient. Thus, the average temperature only weakly impacts the thermal
566 fractionation, but the trend in the temperature history is important.

567 Developing an uncertainty for the trend in the temperature history is not straightforward
568 because it requires making assumptions about the magnitude of timing of temperature
569 change on multi-centennial to millennial timescales. The difference between the main
570 reconstruction and the scaled water isotopes (Figure 8 in the main text) illustrates the
571 uncertainty in these higher frequency trends. Therefore, we seek a simple approximation to
572 capture the main features of the uncertainty to allow comparison with the other sources of
573 uncertainty in determining the thinning function. We assume an uncertainty in the glacial
574 period of 3 m, which is half the maximum impact of including thermal fractionation. To

575 reflect the lower uncertainty due to increasing accumulation rates during the transition
576 into the Holocene, we linearly decrease the uncertainty to 1.5 m from 20 ka to 12 ka,
577 where it is then constant through the present.

578 *S5.2 Total uncertainty on thinning function*

579 To calculate the total uncertainty on the $\delta^{15}\text{N}$ -based thinning function, we combine the
580 uncertainty calculated for each of the seven terms above. The uncertainties for each term
581 are shown in Figure S19. We combine the six sources of uncertainty in quadrature to find
582 the total uncertainty. For glacial-aged ice, the dominant uncertainty is that for Δdepth .
583 This is driven by the larger uncertainty in Δage primarily due to the larger Δage at
584 WAIS Divide during the glacial. During the Holocene, all of the terms are more similar
585 in magnitude, but the uncertainty due to temporal variations in the density profile is the
586 largest. Our use of a uniform value (.023) for temporal density for the full record is likely
587 too simplistic, and perhaps too conservative, since the uncertainty is based on glacial
588 values which differ from modern value far more than the Holocene values.

589 References

- 590 Barkan, E & Luz, B. (2007). Diffusivity fractionations of $\text{H}_2^{16}\text{O}/\text{H}_2^{17}\text{O}$ and $\text{H}_2^{16}\text{O}/\text{H}_2^{18}\text{O}$
591 in air and their implications for isotope hydrology. *Rapid Communications in Mass*
592 *Spectrometry*, 21(18), 2999–3005. <https://doi.org/10.1002/rcm.3180>
- 593 Catania, G, C. Hulbe, & H. Conway, 2010. Grounding-line basal melt rates de-
594 termined using radar-derived internal stratigraphy, *J. Glaciol.* 56(197), 545–554
595 <https://doi.org/10.3189/002214310792447842>
- 596 Cuffey, K. M., & Paterson, W. S. B. (2010). The physics of glaciers. Academic Press.
- 597 Dahl-Jensen, D., Mosegaard, K., Gundestrup, N., Clow, G. D., Johnsen, S. J., Hansen,
598 A. W., & Balling, N. (1998). Past temperatures directly from the Greenland ice sheet.
599 *Science*, 282(5387), 268–271. <https://doi.org/10.1126/science.282.5387.268>
- 600 Dansgaard, W., & Johnsen, S. J. (1969). A flow model and a time scale for the
601 ice core from Camp Century, Greenland. *Journal of Glaciology*, 8(53), 215–223.
602 <https://doi.org/10.3189/S0022143000031208>
- 603 Epifanio, J. A., Brook, E. J., Buizert, C., Edwards, J. S., Sowers, T. A., Kahle, E. C.,
604 Severinghaus, J. P., Steig, E. J., Winski, D. A., Osterberg, E. C., Fudge, T. J., Aydin,
605 M., Hood, E., Kalk, M., Kreutz, K. J., Ferris, D. G., & Kennedy, J. A. (2020). The SP19
606 chronology for the South Pole Ice Core–Part 2: gas chronology, Δage , and smoothing of
607 atmospheric records. *Climate of the Past*, 16(6), 2431–2444. [https://doi.org/10.5194/cp-](https://doi.org/10.5194/cp-16-2431-2020)
608 [16-2431-2020](https://doi.org/10.5194/cp-16-2431-2020)
- 609 Forsberg, R., A.V. Olesen, F. Ferraccioli, T. Jordan, H, Corr, & K. Matsuoka (2017).
610 PolarGap 2015/16: Filling the GOCE polar gap in Antarctica and ASIRAS flight around
611 South Pole. Radar grids available at:

- 612 `ftp://ftp.bas.ac.uk/tomj/PolarGAP/PolarGAP_radar_grids.zip`
- 613 Fudge, T. J., Biyani, S. C., Clemens-Sewall, D., & Hawley, R. L. (2019). Constraining
614 geothermal flux at coastal domes of the Ross Ice Sheet, Antarctica. *Geophysical Research
615 Letters*, 46(22), 13090–13098. <https://doi.org/10.1029/2019GL084332>
- 616 Fudge, T. J., Lilien, D. A., Koutnik, M., Conway, H., Stevens, C. M., Waddington, E. D.,
617 Steig, E. J., Schauer, A. J., & Holschuh, N. (2020). Advection and non-climate impacts
618 on the South Pole Ice Core. *Clim. Past*, 16, 819–832. [https://doi.org/10.5194/cp-16-
619 819-2020](https://doi.org/10.5194/cp-16-819-2020)
- 620 Gades, A. M., Raymond, C. F., Conway, H., & Jacobel, R. W. (2000). Bed
621 properties of Siple Dome and adjacent ice streams West Antarctica, inferred
622 from radio-echo sounding measurements. *Journal of Glaciology*, 46(152), 88–94.
623 <https://doi.org/10.3189/172756500781833467>
- 624 Gelman, A., Roberts, G. & Gilks W. (1996). Efficient Metropolis jumping rules, in
625 Bayesian Statistics 5, Berger, J. O., Bernardo, J. M., Dawid, A. P. and Smith, A.
626 F. M. (eds), Oxford University Press.
- 627 Gkinis, V., Simonsen, S. B., Buchardt, S. L., White, J. W. C., & Vinther, B. M. (2014).
628 Water isotope diffusion rates from the NorthGRIP ice core for the last 16,000 years -
629 glaciological and paleoclimatic implications. *Earth and Planetary Science Letters*, 405,
630 132–141. <https://doi.org/10.1016/j.epsl.2014.08.022>
- 631 Gkinis, V., Holme, C., Kahle, E.C., Stevens, C.M., Steig, E.J., & Vinther, B.M. (2021).
632 Numerical experiments on firn isotope diffusion with the Community Firn Model. *Jour-
633 nal of Glaciology*, 1–23. doi:10.1017/jog.2021.1

- 634 Goujon, C., Barnola, J. M., & Ritz, C. (2003). Modeling the densification of polar firn in-
635 cluding heat diffusion: Application to close-off characteristics and gas isotopic fractiona-
636 tion for Antarctica and Greenland sites. *Journal of Geophysical Research: Atmospheres*,
637 108(D24). <https://doi.org/10.1029/2002JD003319>
- 638 Grachev, A. M., & Severinghaus, J. P. (2003). Laboratory determination of thermal dif-
639 fusion constants for $^{29}\text{N}_2/^{28}\text{N}_2$ in air at temperatures from 60 to 0 C for reconstruction
640 of magnitudes of abrupt climate changes using the ice core fossil–air paleothermome-
641 ter. *Geochimica et Cosmochimica Acta*, 67(3), 345–360. [https://doi.org/10.1016/S0016-](https://doi.org/10.1016/S0016-7037(02)01115-8)
642 [7037\(02\)01115-8](https://doi.org/10.1016/S0016-7037(02)01115-8)
- 643 Herron, M. M., & Langway, C. C. (1980). Firn densification: an empirical model. *Journal*
644 *of Glaciology*, 25(93), 373–385. <https://doi.org/10.3189/S0022143000015239>
- 645 Johnsen, S. J., Clausen, H. B., Cuffey, K. M., Hoffmann, G., Schwander, J., & Creyts,
646 T. (2000). Diffusion of stable isotopes in polar firn and ice: The isotope effect in firn
647 diffusion. T. Hondoh (Ed.), *Physics of Ice Core Records*, Hokkaido University Press,
648 Sapporo (2000), pp. 121–140.
- 649 Jones, T. R., White, J. W. C., Steig, E. J., Vaughn, B. H., Morris, V., Gkinis, V.,
650 Markle, B. R., & Schoenemann, S. W. (2017b). Improved methodologies for continuous
651 flow analysis of stable water isotopes in ice cores. *Atmospheric Measurement Techniques*,
652 10, 617–632. <https://doi.org/10.5194/amt-10-617-2017>
- 653 Jordan, T. A., Martin, C., Ferraccioli, F., Matsuoka, K., Corr, H., Forsberg, R., Ole-
654 sen, A., & Siegert, M. (2018). Anomalously high geothermal flux near the South Pole.
655 *Scientific reports*, 8(1), 1–8. <https://doi.org/10.1038/s41598-018-35182-0>

- 656 Kahle, E. C. (2020). Climate reconstructions from ice cores: New techniques to un-
657 derstand the information preserved in the South Pole ice core (Doctoral dissertation,
658 University of Washington, Seattle, USA). <http://hdl.handle.net/1773/45398>
- 659 Khan, A., Mosegaard, K., & Rasmussen, K. L. (2000). A new seismic velocity model for
660 the Moon from a Monte Carlo inversion of the Apollo lunar seismic data. *Geophysical*
661 *Research Letters*, 27(11), 1591–1594. <https://doi.org/10.1029/1999GL008452>
- 662 Koutnik, M. R., Fudge, T. J., Conway, H., Waddington, E. D., Neumann, T. A., Cuffey,
663 K. M., Taylor, K. C., et al. (2016). Holocene accumulation and ice flow near the West
664 Antarctic Ice Sheet Divide ice core site. *Journal of Geophysical Research: Earth Surface*,
665 121(5), 907–924. <https://doi.org/10.1002/2015JF003668>
- 666 Lamb, K. D., Clouser, B. W., Bolot, M., Sarkozy, L., Ebert, V., Saathoff, H., Mohler, O.,
667 & Moyer, E. J. (2017). Laboratory measurements of HDO/H₂O isotopic fractionation
668 during ice deposition in simulated cirrus clouds. *Proceedings of the National Academy*
669 *of Sciences*, 114(22), 5612–5617. <https://doi.org/10.1073/pnas.1618374114>
- 670 Li, J. & Zwally, H. J. (2015). Response times of ice-sheet surface heights to changes in the
671 rate of Antarctic firn compaction caused by accumulation and temperature variations.
672 *Journal of Glaciology*, 61(230), 1037–1047. <https://doi.org/10.3189/2015JoG14J182>
- 673 Ligtenberg, S. R. M., Helsen, M. M., & Van den Broeke, M. R. (2011). An improved
674 semi-empirical model for the densification of Antarctic firn. *The Cryosphere*, 5, 809–
675 819. <https://doi.org/10.5194/tc-5-809-2011>
- 676 Lilien, D. A., Fudge, T. J., Koutnik, M. R., Conway, H., Osterberg, E. C.,
677 Ferris, D. G., & Stevens, C. M. et al. (2018). Holocene Ice-Flow Speedup in
678 the Vicinity of the South Pole. *Geophysical Research Letters*, 45(13), 6557–6565.

- 679 <https://doi.org/10.1029/2018GL078253>
- 680 Looyenga, H. (1965). Dielectric constants of heterogeneous mixtures. *Physica*, 31(3), 401–
681 406. [https://doi.org/10.1016/0031-8914\(65\)90045-5](https://doi.org/10.1016/0031-8914(65)90045-5)
- 682 Luz, B. & Barkan, E. (2010). Variations of 17O/16O and 18O/16O in
683 meteoric waters. *Geochimica et Cosmochimica Acta*, 74(22), 6276–6286.
684 <https://doi.org/10.1016/j.gca.2010.08.016>
- 685 Majoube, B. (1970). Fractionation factor of ¹⁸O between water vapour and ice. *Nature*
686 226, 1242. <https://doi.org/10.1038/2261242a0>
- 687 Metropolis, N., Rosenbluth, A. W., Rosenbluth, M. N., Teller, A. H., & Teller, E. (1953).
688 Equation of state calculations by fast computing machines. *The Journal of Chemical*
689 *Physics*, 21(6), 1087–1092. <https://doi.org/10.1063/1.1699114>
- 690 Mosegaard, K. & Tarantola, A. (1995). Monte Carlo sampling of solutions to in-
691 verse problems. *Journal of Geophysical Research: Solid Earth*, 100(B7), 12431–12447.
692 <https://doi.org/10.1029/94JB03097>
- 693 Mosegaard, K. (1998). Resolution analysis of general inverse problems through inverse
694 Monte Carlo sampling. *Inverse Problems*, 14(3), 405. [https://doi.org/10.1088/0266-](https://doi.org/10.1088/0266-5611/14/3/004)
695 [5611/14/3/004](https://doi.org/10.1088/0266-5611/14/3/004)
- 696 Mosegaard, K., & Tarantola, A. (2002). Probabilistic approach to inverse problems. In
697 W. Lee, P. Jennings, C. Kisslinger, & H. Kanamori (Eds.), *International Handbook of*
698 *Earthquake & Engineering Seismology (Part A)* (237–265). Academic Press.
- 699 Mosegaard, K. & Sambridge, M. (2002). Monte Carlo analysis of inverse problems. *Inverse*
700 *problems*, 18(3), R29. <https://doi.org/10.1088/0266-5611/18/3/201>

- 701 Neumann, T. A., Conway, H., Price, S., Waddington, E. D., & Morse, D. L. (2008).
702 Holocene accumulation and ice-sheet dynamics in central West Antarctica. *Journal of*
703 *Geophysical Research*, 113(F2). <https://doi.org/10.1029/2007JF000764>
- 704 Nye, J. 1963. Correction factor for accumulation measured by the thickness
705 of the annual layers in an ice sheet. *Journal of Glaciology*, 4(36), 785–788.
706 <https://doi.org/10.3189/S0022143000028367>
- 707 Parrenin, F., Remy, F., Ritz, C., Siegert, M. J., & Jouzel, J. (2004). New modeling of the
708 Vostok ice flow line and implication of the glaciological chronology of the Vostok ice core.
709 *Journal of Geophysical Research*, 109, (D20). <https://doi.org/10.1029/2004JD004561>
- 710 Parrenin, F., Barker, S., Blunier, T., Chappellaz, J., Jouzel, J., Landais, A., Veres, D.
711 et al. (2012). On the gas-ice depth difference (Δ_{depth}) along the EPICA Dome C ice
712 core. *Climate of the Past*, 8(2), 1089–1131. <https://doi.org/10.5194/cpd-8-1089-2012>
- 713 Price, P. B., Nagornov, O. V., Bay, R., Chirkin, D., He, Y., Miocinovic, P.,
714 Richards, A., Woschnagg, K., Koci, B., & Zagorodnov, V. (2002). Temperature
715 Profile for Glacial Ice at the South Pole: Implications for Life in a Nearby Sub-
716 glacial Lake. *Proceedings of the National Academy of Sciences*, 99(12), 7844–7847.
717 <https://doi.org/10.1073/pnas.082238999>
- 718 Raymond, C. (1983). Deformation in the vicinity of ice divides. *Journal of Glaciology*,
719 29(103), 357–373. <https://doi.org/10.3189/S0022143000030288>
- 720 Schwander, J., Stauffer, B., & Sigg, A. (1988). Air mixing in firn and
721 the age of the air at pore close-off. *Annals of Glaciology*, 10, 141–145.
722 <https://doi.org/10.3189/S0260305500004328>

- 723 Simonsen, S. B., Stenseng, L., Adalgeirsdottir, G., Fausto, R. S., Hvidberg, C. S., &
724 Lucas-Picher, P. (2013). Assessing a multilayered dynamic firn-compaction model for
725 Greenland with ASIRAS radar measurements. *Journal of Glaciology*, 59 (215), 545–558.
726 <https://doi.org/10.3189/2013JoG12J158>
- 727 Steen-Larsen, H. C., Waddington, E. D., & Koutnik, M. R. (2010). Formulating an
728 inverse problem to infer the accumulation-rate pattern from deep internal layering in
729 an ice sheet using a Monte Carlo approach. *Journal of Glaciology*, 56(196), 318–332.
730 <https://doi.org/10.3189/002214310791968476>
- 731 Stevens, C. M., Verjans, V., Lundin, J., Kahle, E. C., Horlings, A. N., Horlings, B. I.,
732 & Waddington, E. D. (2020). The Community Firn Model (CFM) v1. 0. *Geoscientific*
733 *Model Development*, 13(9), 4355–4377. <https://doi.org/10.5194/gmd-13-4355-2020>
- 734 Tarantola, A. (1987). Inverse problem theory: Methods for data fitting and model pa-
735 rameter estimation. *Elsevier Science*, Amsterdam.
- 736 Winski, D. A., Fudge, T. J., Ferris, D. G., Osterberg, E. C., Fegyveresi, J. M., Cole-Dai,
737 J., Buizert, C. et al. (2019). The SP19 chronology for the South Pole Ice Core–Part 1:
738 volcanic matching and annual layer counting. *Climate of the Past*, 15(5), 1793–1808.
739 <https://doi.org/10.5194/cp-15-1793-2019>

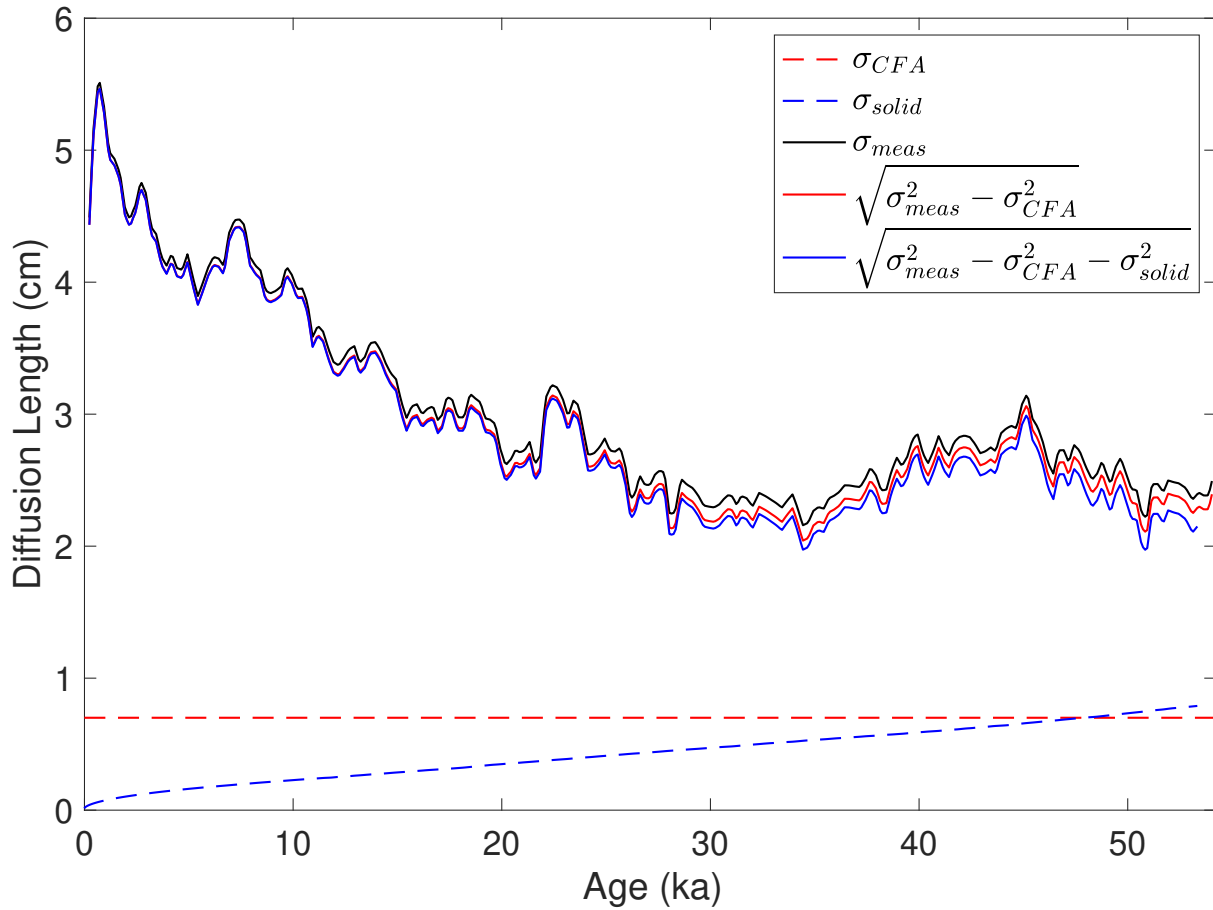


Figure S1: Impact of corrections applied to diffusion-length measurements. Dashed curves show the effective diffusion length resulting from the continuous-flow system (CFA, red), and from diffusion in solid ice (blue). Solid curves show diffusion lengths obtained from the water-isotope data before (black) and after correction for the CFA (red) and solid-ice diffusion (blue).

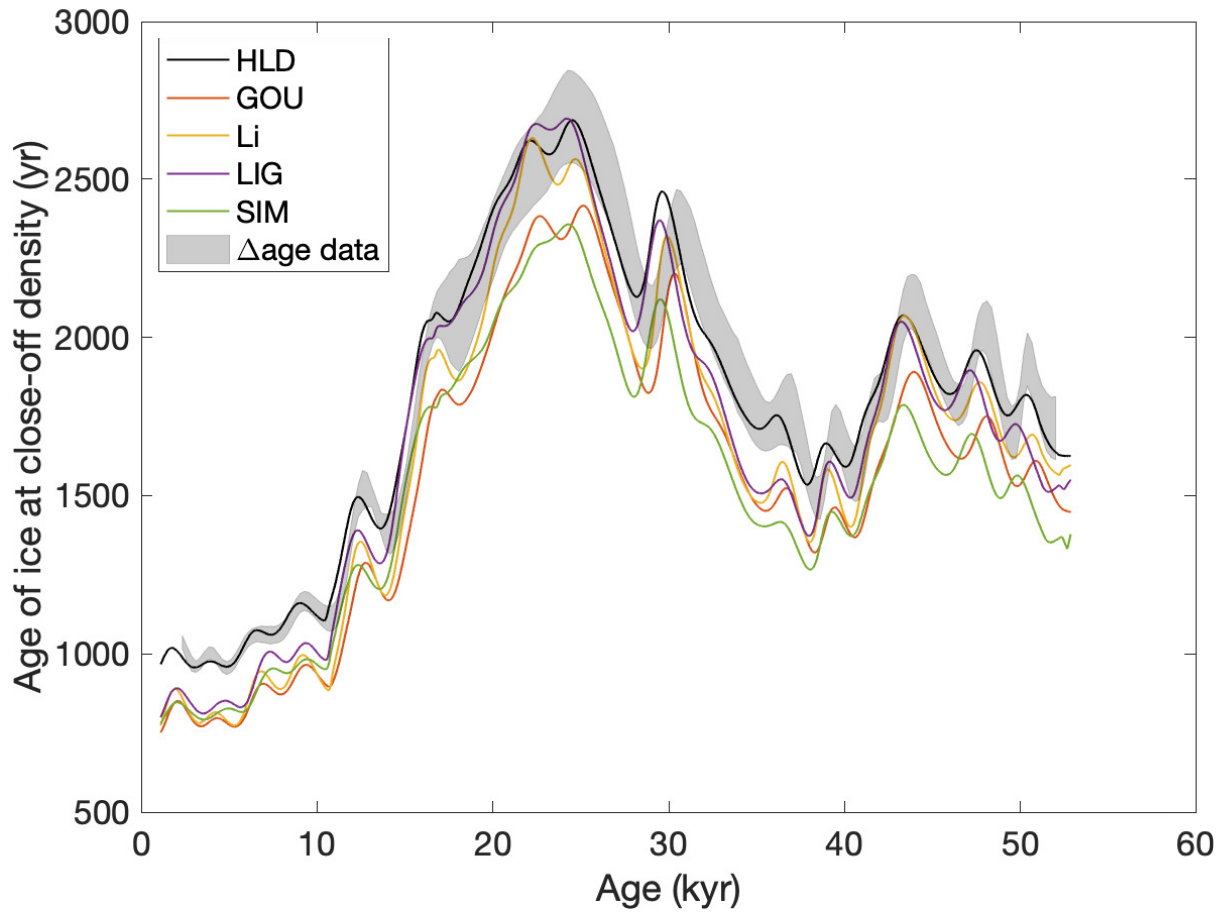


Figure S2: Close-off age as a function of age for a collection of models from the Community Firn Model framework (HLD = Herron and Langway (1980), GOU = Goujon et al. (2003), Li = Li and Zwally (2015), LIG = Ligtenberg et al. (2011), SIM = Simonsen et al. (2013)). The grey shading shows the Δ age data and two s.d. uncertainty.

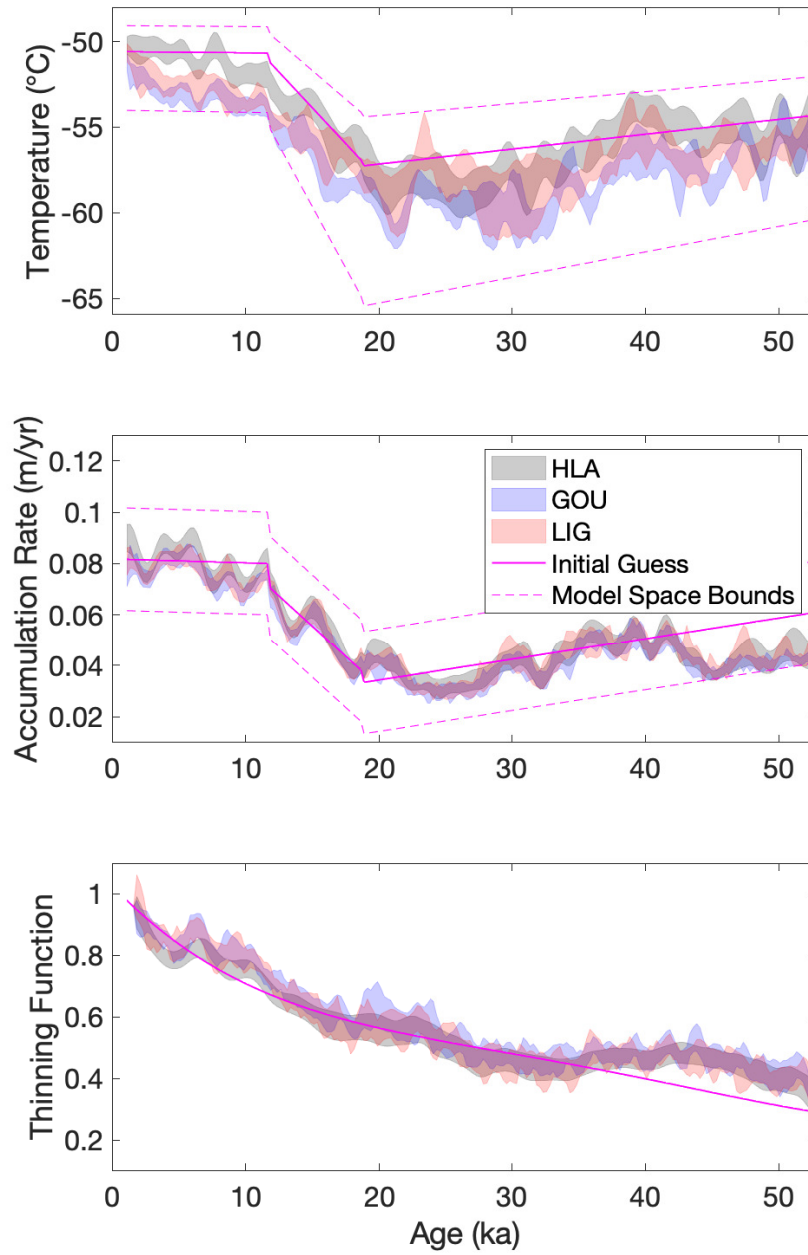


Figure S3: Results of inverse procedure using three different firn models. Grey, blue, and red shading show two s.d. results for Herron and Langway (1980) (HLA), Goujon et al. (2003) (GOU), and Ligtenberg et al. (2011) (LIG), respectively.

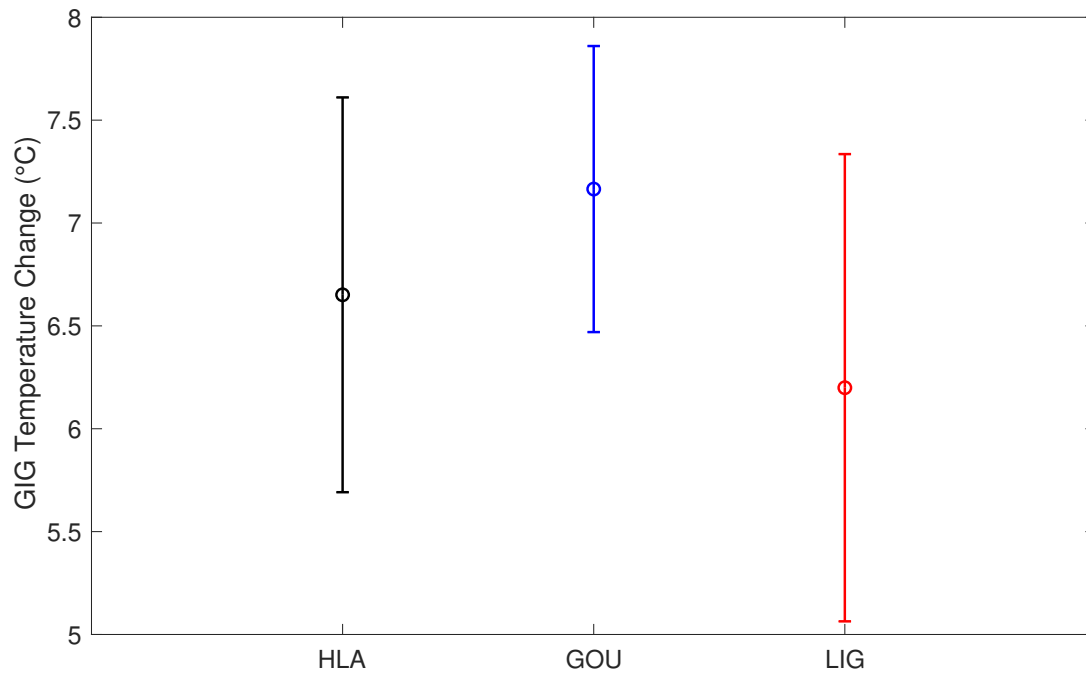


Figure S4: Glacial-interglacial temperature change from the inverse framework with three different firn models. Mean and one s.d. are shown for Herron and Langway (1980) (HLA), Goujon et al. (2003) (GOU), and Ligtenberg et al. (2011) (LIG). The temperature difference is calculated on the intervals defined in the main text: present = 500-2500 years; glacial = 19500-22500 years. The temperature reconstructions have been corrected for ice advection from upstream, resulting in a temperature change estimate for the South Pole site.

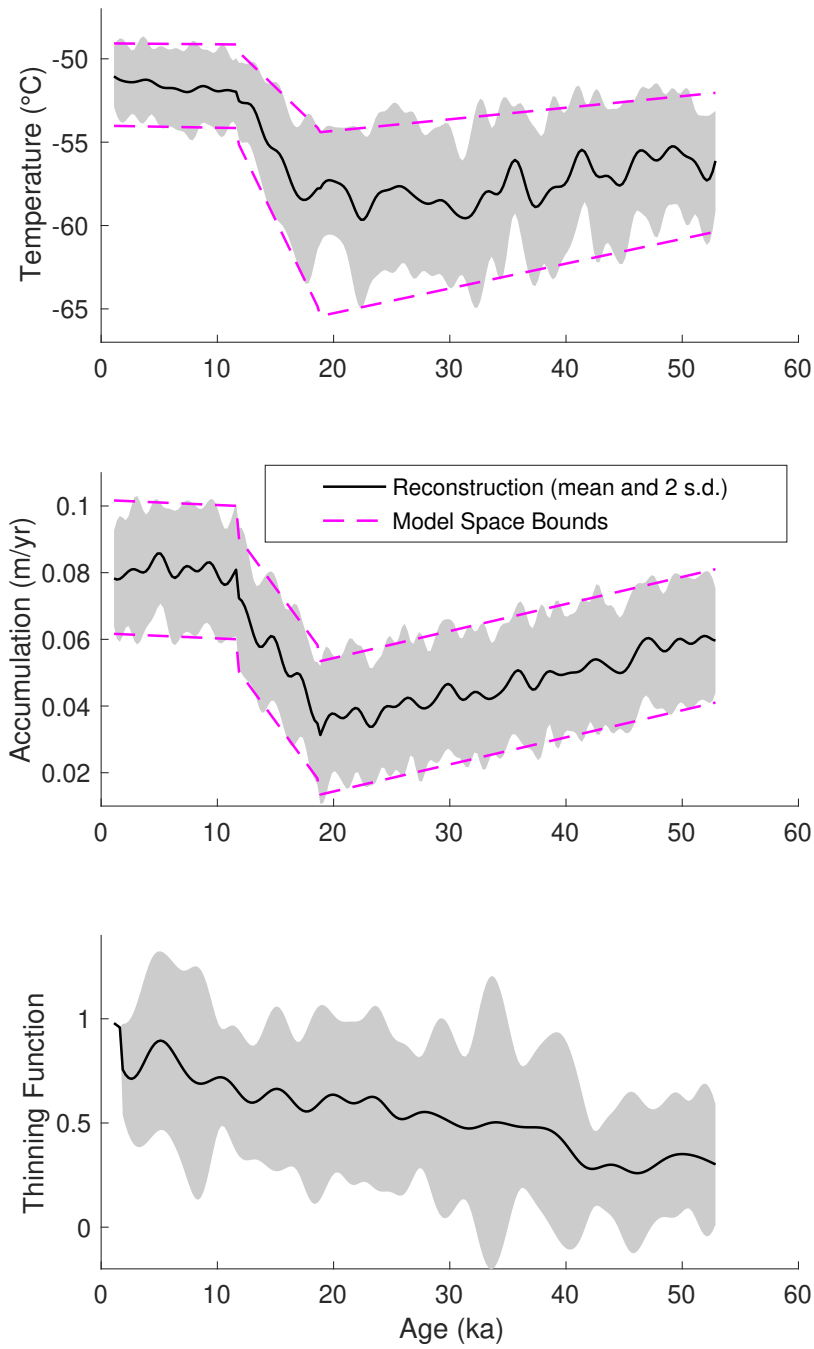


Figure S5: Results of the null test to recover the *a priori* distribution. In the upper two panels, for which model bounds are defined, two standard deviations of the *a posteriori* distribution (grey shading) approximately fill the bounded space (dashed magenta lines), and the mean of the distribution (black curve) is approximately the mean of the bounds.

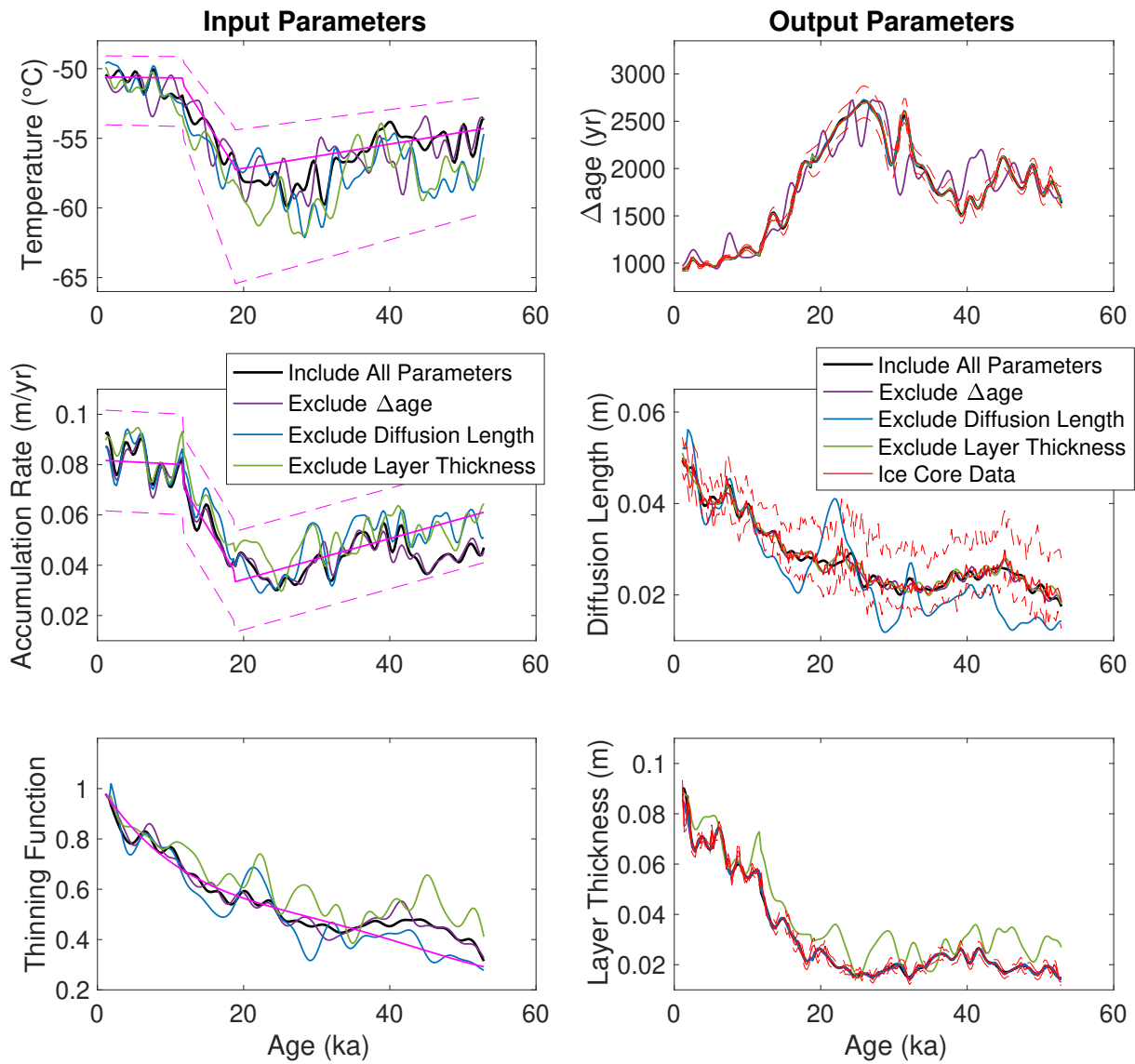


Figure S6: Analysis of the sensitivity of the *a posteriori* distribution to information in each data set. Each color shows the *a posteriori* distribution mean for a different sensitivity test. We compare the results when Δage is excluded (purple), when diffusion length is excluded (blue), when layer thickness is excluded (green), and when all data sets are included (black). Magenta curves in the left panels show *a priori* information and red curves in the right panels show ice-core data and uncertainties.

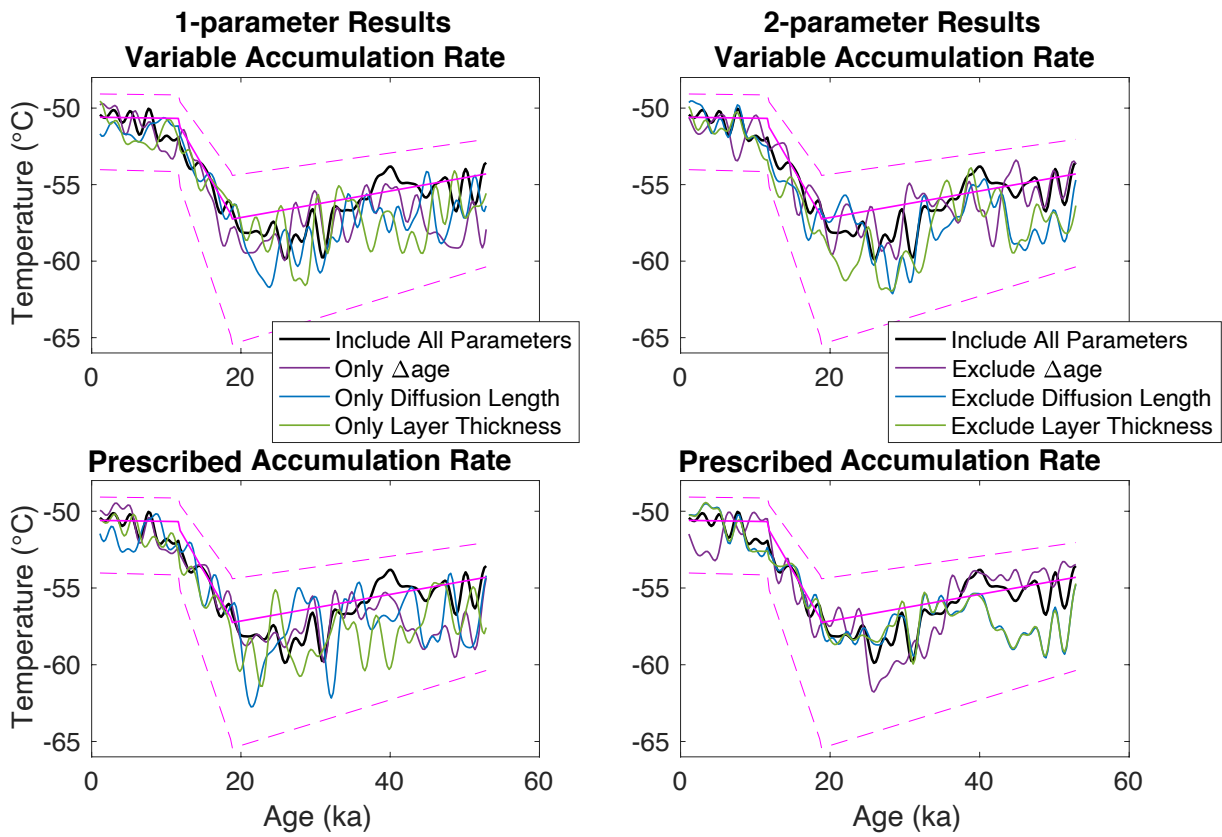


Figure S7: Analysis of the sensitivity of temperature to information in each data set. Colors are defined as in Figure S6. The results of the 1-parameter suite are shown on the left and of the 2-parameter suite on the right. The upper row shows the result when accumulation rate is allowed to vary, and the lower row shows the result when accumulation rate is held at the prescribed values.

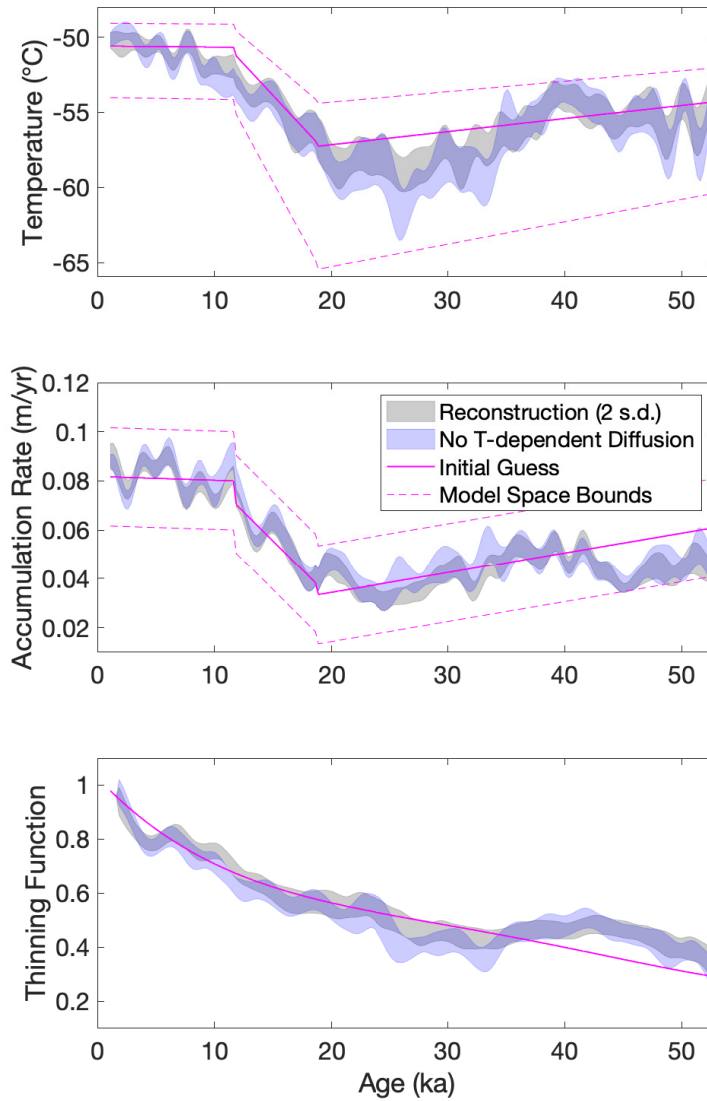


Figure S8: Analysis of sensitivity to the temperature dependence within the water-isotope diffusion model. Grey shading shows the main inverse result as a control test. Blue shading shows the results from holding the temperature history constant within the water-isotope diffusion model, only allowing the diffusion-length data to impact the thinning function.

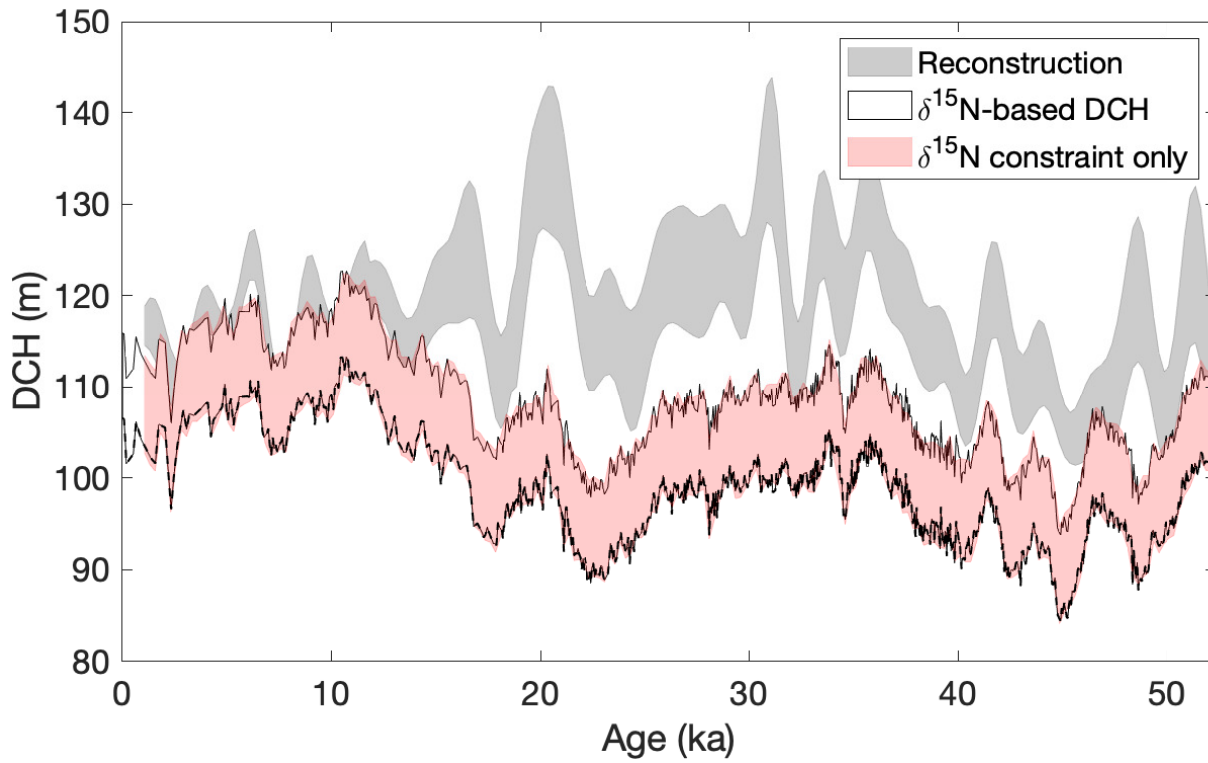


Figure S9: Comparison of diffusive column height (DCH), shown as two s.d. for each source. Grey shading shows the DCH as modeled by the temperature and accumulation rate solutions accepted in the main reconstruction. The black outline shows the DCH as calculated from the $\delta^{15}\text{N}$ data. Red shading shows the $\delta^{15}\text{N}$ -constrained DCH, reconstructed from the temperature and accumulation-rate histories shown in Figure 5 in the main text.

Table S1: Sensitivity of the relationship between water isotopes and temperature. Calibrated slopes are given for the relationship between water isotopes and temperature from five different temperature reconstructions: the main inverse result, the results from using the GOU and LIG firn models instead of HLA, and the results from using the constraints of the $\delta^{15}\text{N}$ and Δage data sets. The correlation coefficient r is given for the relationship between the water-isotope record and each temperature reconstruction.

Reconstruction	Slope ($\text{‰}^\circ\text{C}^{-1}$)	r
Main	0.99	0.94
GOU	0.97	0.94
LIG	1.10	0.90
$\delta^{15}\text{N}$	1.28	0.84
$\delta^{15}\text{N}$ & Δage	1.14	0.86

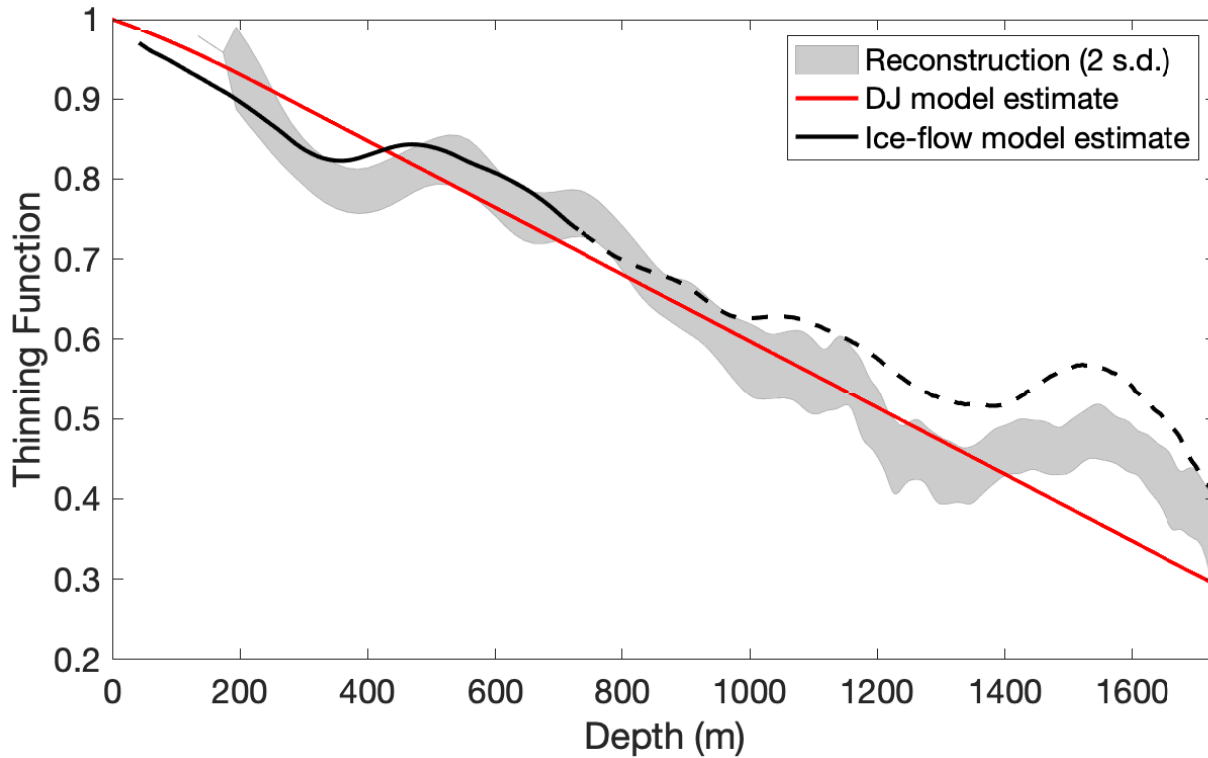


Figure S10: Comparison of primary thinning reconstruction (grey band shows two s.d. uncertainty), the 1-D Dansgaard-Johnsen model output (red) plotted against depth, and the thinning estimate from the 2.5-D ice flow model (black). As in Figure 6 in the main text, the dashed black line shows the depths at which the upstream bed topography is unknown. The reconstruction shows considerably more high-frequency variability. Note that the reconstruction band collapses to a line at the upper depth points due to an imposed constraint of *a priori* information to limit variability in the uppermost part of the thinning function.

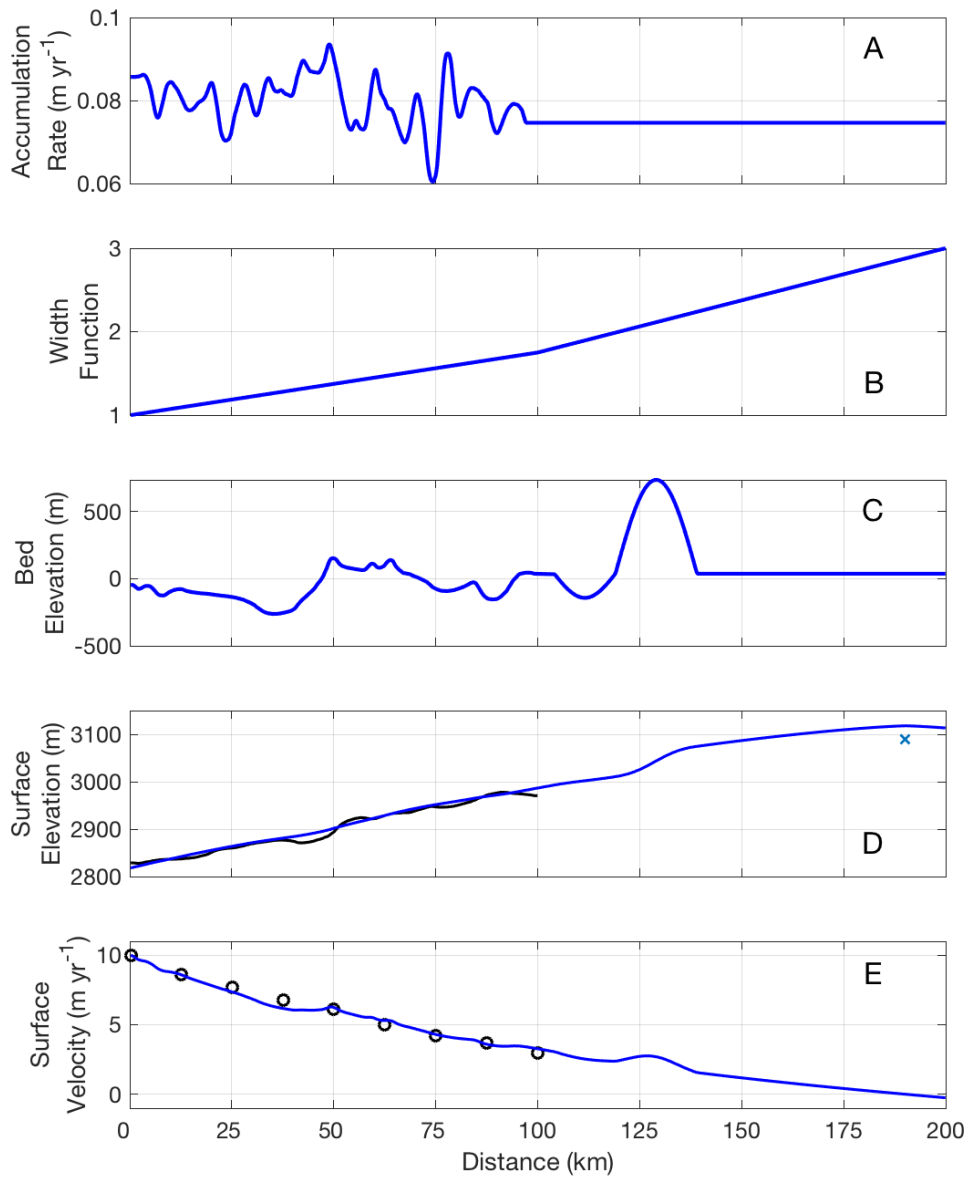


Figure S11: Flowband model inputs (A-C) and model fits to measured data (D-E). A) Modern accumulation-rate pattern for 100 km upstream of SPC14 site inferred from the available shallow radar measurements (Lilien et al., 2018; Fudge et al., 2020). B) Normalized width function used to fit measured surface velocities in panel E. C) Bed topography was measured from 0 to 100 km. Beyond 100 km, the bed topography used in the model is determined as discussed in Text S4.2. D) Measured (black) and modeled surface elevation (blue). The small black “x” at 190 km marks the approximate position and elevation of Titan Dome relative to SPC14. E) Measured (black circles) and modeled surface velocities (blue).

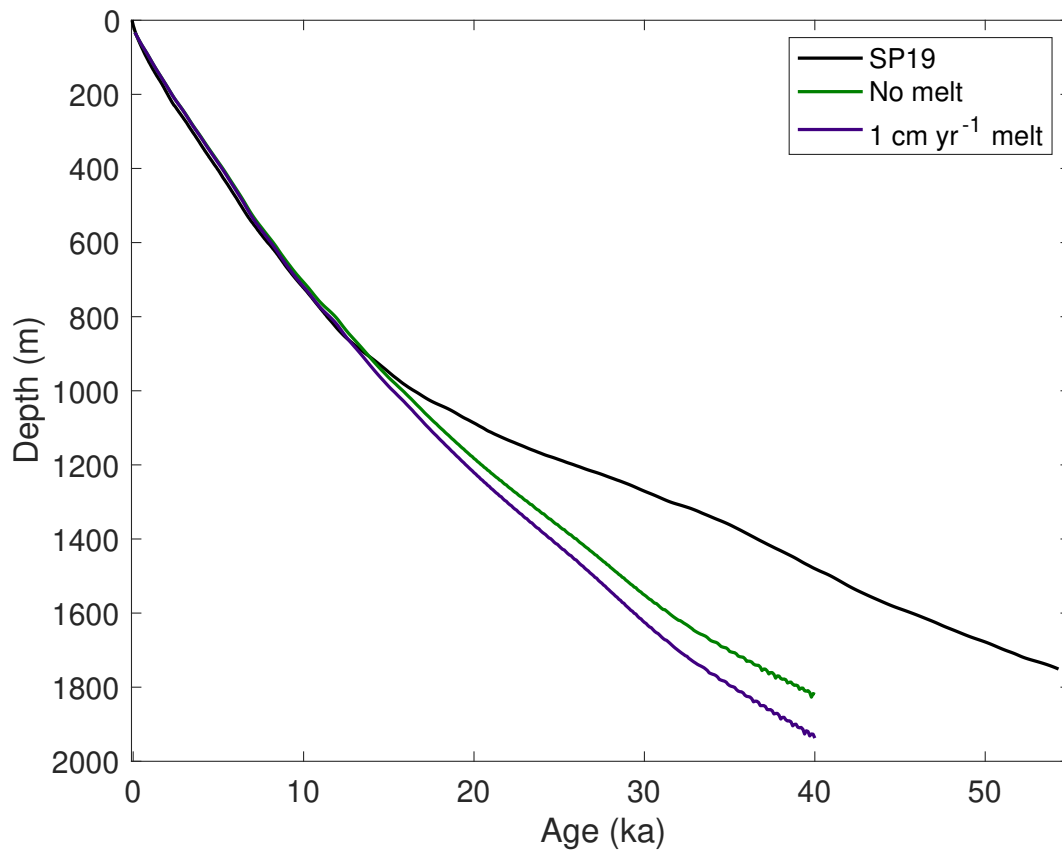


Figure S12: Comparison between modeled and measured depth-age relationship. The depth-age relationship from the steady-state models compare well to SP19 (Winski et al., 2019) for the Holocene. The divergence in the modeled values compared to SP19 values below approximately 900 m depth is due to the decrease in accumulation rate at older ages that we do not simulate with the steady-state model.

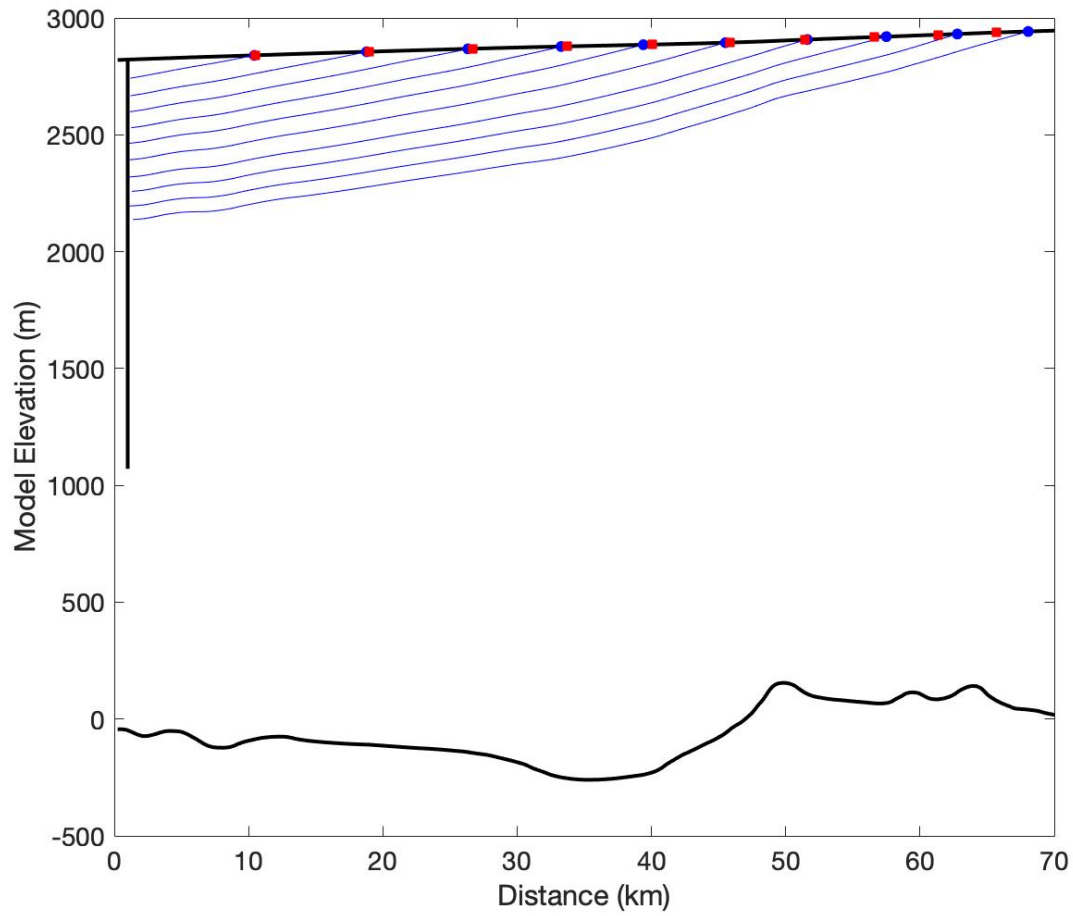


Figure S13: The origin location of ice parcels in 1 ka increments are shown in red squares for the reconstruction of Lilien et al. (2018) and the flowband model used in this study (blue dots). The blue lines are the modeled ice parcel paths. The black vertical line at 1 km represents the 1751 m deep SPC14.

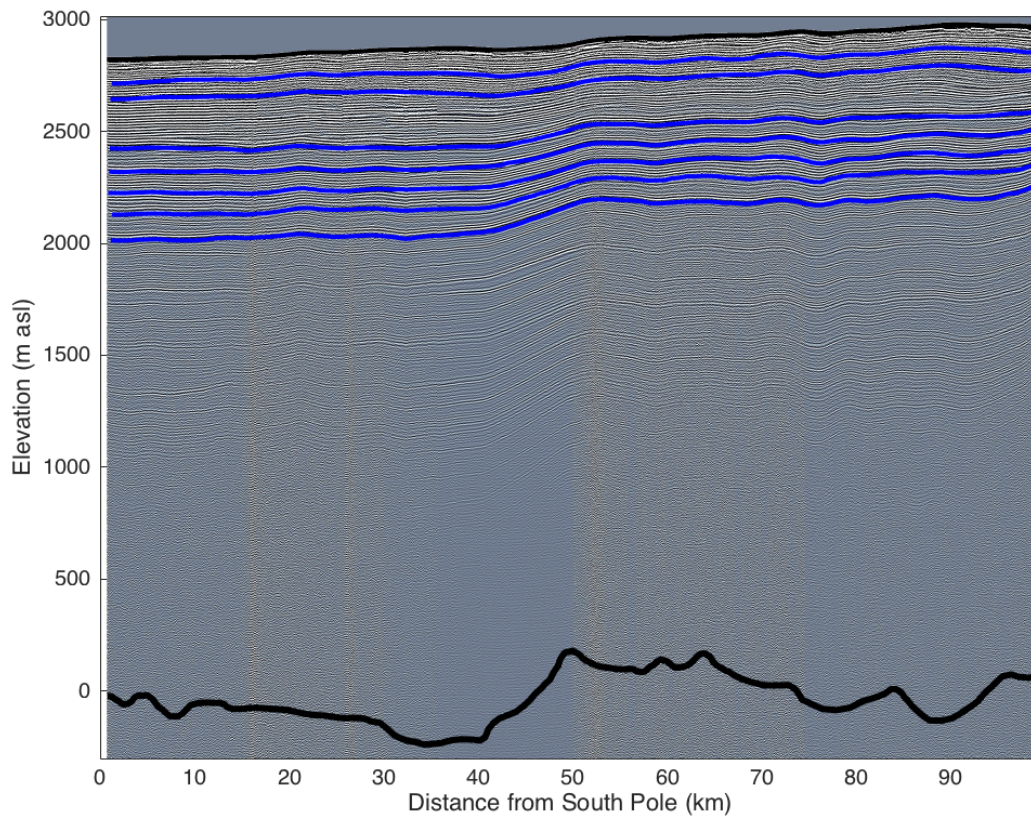


Figure S14: Radar profile along 100 km of the modern flowline upstream of SPC14 (see map, Figure S16). The data were imaged using a ground-based, bistatic impulse radar with center frequency of 7 MHz. The transmitter and receiver were towed inline behind a skidoo; each record consists of 1024 stacked waveforms and records were located using GPS. Reflection positions, measured as a function of radar two-way travel time, were converted to depth below the surface using a wave speed of $168.5 \text{ m } \mu\text{s}^{-1}$ in ice and $300 \text{ m } \mu\text{s}^{-1}$ in air. Wave speed in the firn was calculated using the density profile from SPC14 and a mixing equation (Looyenga, 1965) to estimate the depth profile of the dielectric constant. Solid black curves show the surface and bed elevations (m above sea level (asl)). Note that the SPC14 site is about 40 m below sea level. Blue curves are radar-detected internal layers (isochrones) that were dated using the SPC14 timescale. Layer ages with increasing depth are: 1020, 1900, 5070, 6510, 8070, 9690, and 11770 years.

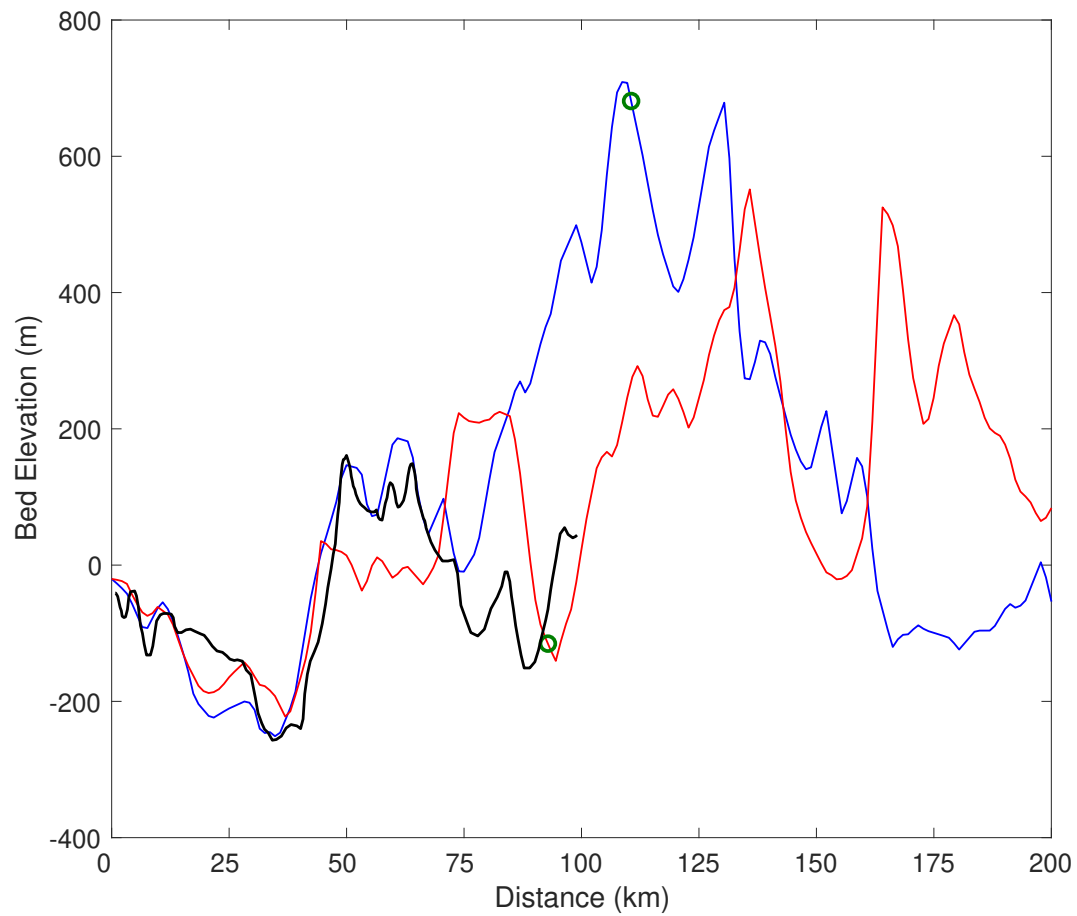


Figure S15: Profiles of bed topography upstream of the SPC14 site. Black is the bedrock measured along the modern flowline. Red is along 142.5° E and blue is along 135° E from the PolarGAP survey. Green circles mark the two points that we use to define a plausible bed feature to explain the thinning function for older ages (circles correspond to Figure S16).

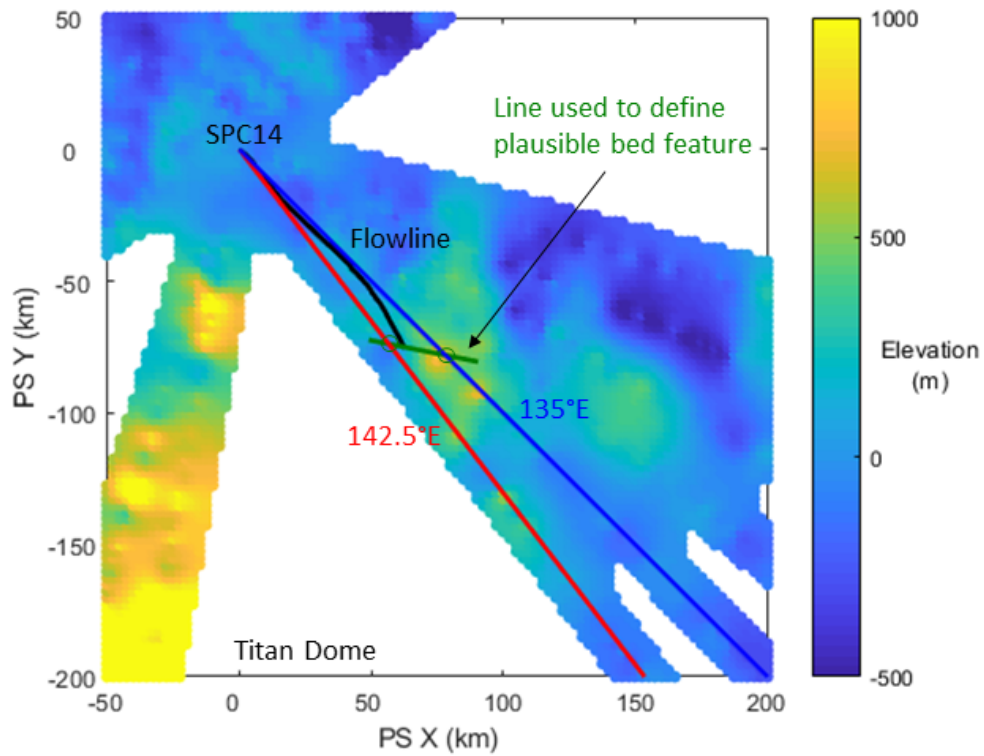


Figure S16: Map view of bed topography near SPC14. Black shows measured flowline. Red is along 142.5° E and blue is along 135° E from the PolarGAP survey. Green line shows the transect between PolarGAP lines used to guide the bed topographic feature beyond 100 km in the ice-flow modeling (circles correspond to Figure S15).

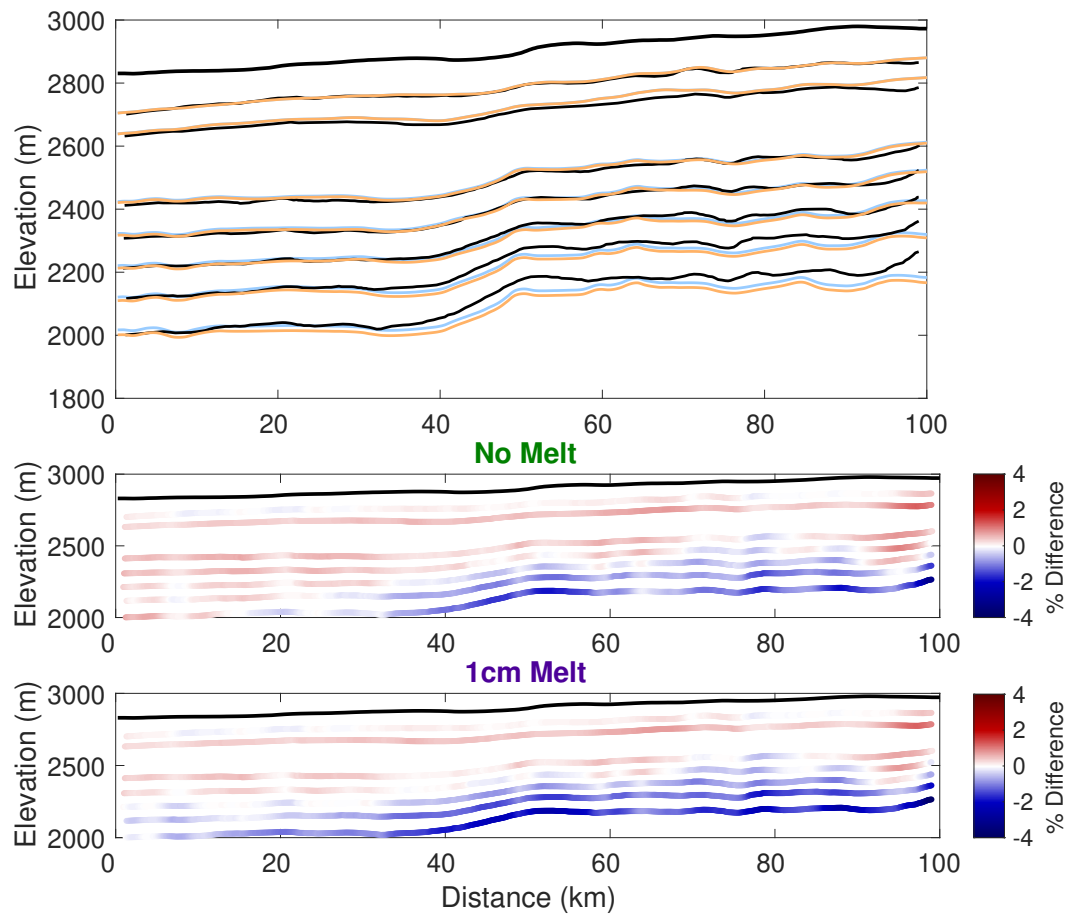


Figure S17: Comparison between modeled and measured internal layers in the flowband domain. Measured layers are shown in Figure S14. A) Observed (black) and modeled with no melt (blue) and 1 cm a⁻¹ melt (orange) internal layers. Observed layer ages are labeled. B) Percent misfit of layer depths for the “no melt” model. C) Percent misfit of layer depths for the “1 cm a⁻¹ melt” model.

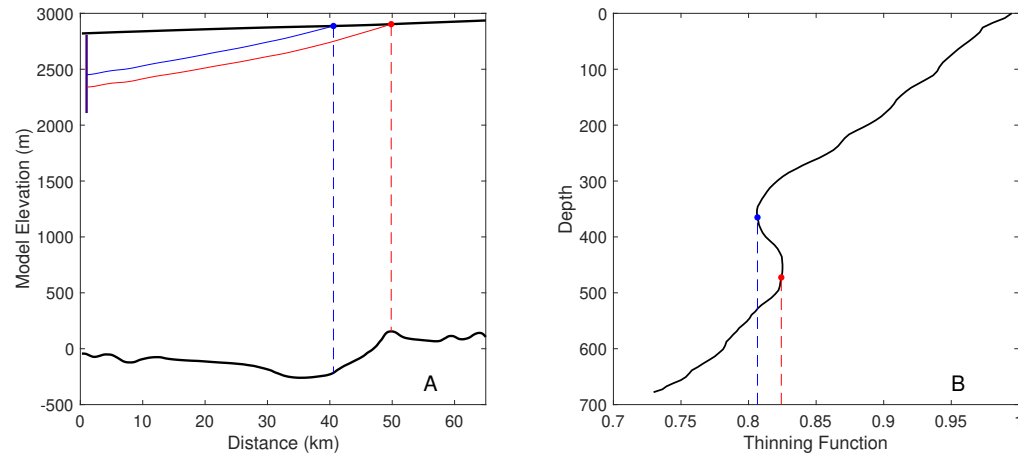


Figure S18: Illustration of the development of a reversal in the thinning function. A) Modeled particle paths with ice thickness (and corresponding bed elevation) at particle origin marked. Age of the red particle is ~ 7 ka and age of the blue particle is ~ 6 ka. Purple vertical line at the far left side is ice-core location and the depth of the core shows the depth range plotted in B. B) Modeled thinning function showing the reversal in thinning due to thickening of the ice sheet which the red particle experienced by the blue particle did not. The jaggedness of the thinning function is due to numerical challenges in the particle tracking.

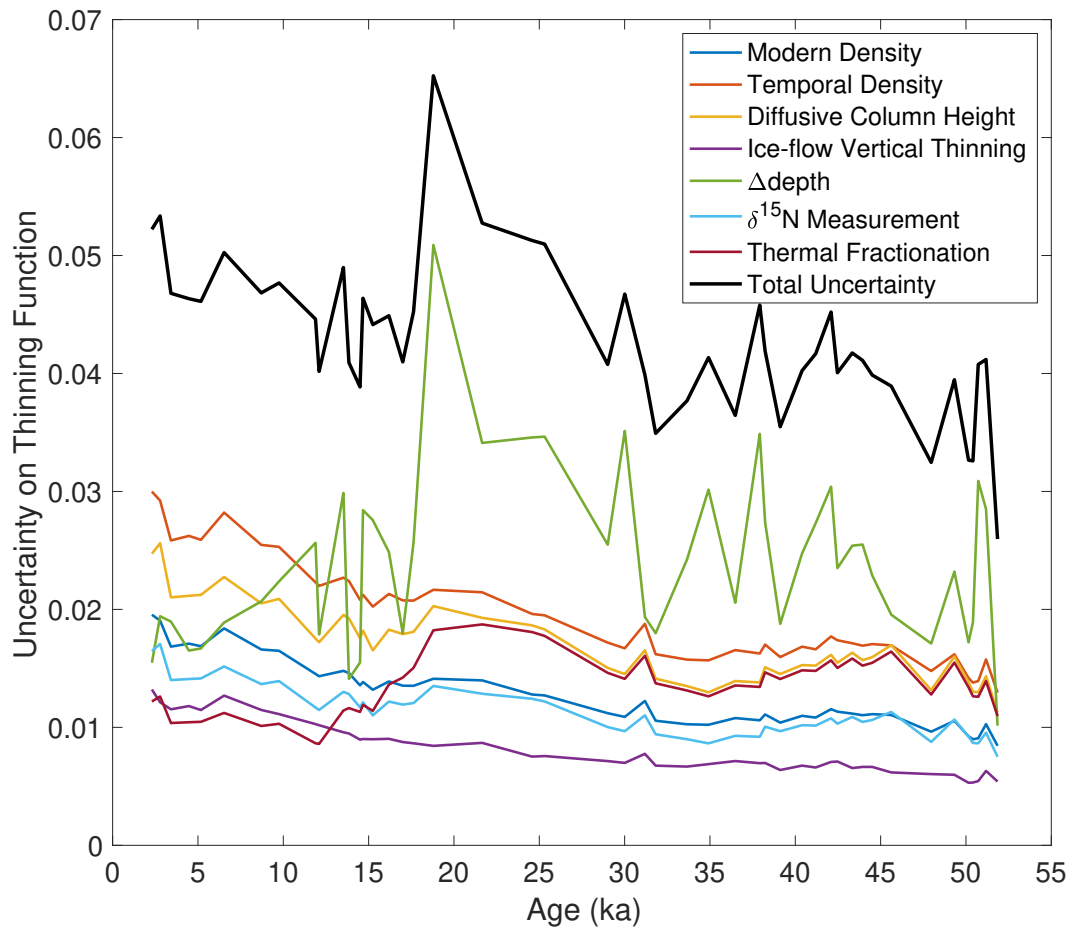


Figure S19: Uncertainty representing two standard deviations for the inferred thinning function from seven main sources described in Text S5.1.